J. Fluid Mech. (2009), *vol.* 619, *pp.* 331–365. © 2008 Cambridge University Press
doi:10.1017/S0022112008004564 Printed in the United Kingdom

Electrokinetic instabilities of non-dilute colloidal suspensions

GURU NAVANEETHAM[1] AND JONATHAN D. POSNER[1,2]†
[1]Department of Mechanical Engineering, Arizona State University, Tempe, AZ, USA
[2]Department of Chemical Engineering, Arizona State University, Tempe, AZ, USA

(Received 31 August 2007 and in revised form 30 September 2008)

An experimental investigation of electrokinetic instabilities (EKIs) of non-dilute colloidal suspensions in microchannels is presented. The addition of charged colloidal particles to a solution can alter the solution's electrical conductivity and permittivity as well as the average particle electrophoretic mobility. In this work, a colloidal (500 nm polystyrene) volume fraction gradient is achieved at the intersection of a Y-shaped polydimethylsiloxane (PDMS) microchannel. The flow becomes unstable when the electroviscous stretching and folding of the conductivity and permittivity interfaces exceed the dissipative effects of viscous forces and particle diffusion. The suspension conductivity as a function of the particle volume fraction is presented. The critical conditions required for flow instability are measured along with a scaling analysis which shows that the flow becomes unstable due to a coupling of applied electric fields and the electrical conductivity and permittivity gradients in the flow. The flow becomes unstable at a critical electric Rayleigh number of $Ra_e = 1.8 \times 10^5$ for a wide range of applied electric fields spanning three orders of magnitude and colloid volume fractions varying two orders of magnitude. EKIs of non-dilute colloidal suspensions may be important for applications such as the electrophoretic deposition of micropatterned colloidal assemblies, electrorheological devices and on-chip electrokinetic (EK) manipulation of colloids.

1. Introduction

The transport of non-dilute colloidal suspensions under externally applied electric fields are important in a number of applications such as electrorheology (see Ikazaki *et al.* 1998; Espin, Delgado & Rejon 2005), field-induced pattern formations in colloidal dispersions (see Trau *et al.* 1995; Whitesides & Grzybowski 2002), field-induced layering of colloidal crystals films, patterned microarrays (see Trau, Saville & Aksay 1996; Hayward, Saville & Aksay 2000), electronic chip cooling (see Jang & Choi 2006) and field-induced separations, viz. field-induced flow fractionation and dielectrophoresis systems. In addition, recent work in microfluidic and nanofluidic systems have focused on the electrokinetic injection, separation, concentration and mixing of charged particles or analytes, where non-dilute volume fractions of charged species may be encountered locally (see Stone & Kim 2001; Bazant & Squires 2004).

Electrokinetics is a branch of electrohydrodynamics that describes the transport of ions, fluid flow and their interactions with electric fields and is distinguished from

---

† Email address for correspondence: jposner@asu.edu

electrohydrodynamics by the presence of charges at the interface of the solid–liquid boundaries (see Saville 1997). Two important classes of electrokinetic (EK) flow are electrophoresis and electro-osmosis, wherein the motion of charge stabilized colloidal particles and fluids, respectively, occurs when an external electric field is applied to the system (see Probstein 1994). EK flows in microscale channels and around charged particles are strongly damped by viscous forces and typically laminar with Reynolds numbers less than unity.

It has been shown that flows with electric fields coupled with gradients in ionic conductivity can, under certain conditions, become unstable. These instabilities were first observed by Melcher in the late 1960s (see Melcher & Taylor 1969). Hoburg & Melcher (1976) performed experiments in dielectric liquids (corn oil) in which they applied an electric field transverse to the conductivity gradients, which always resulted in electrohydrodynamic (EHD) instabilities. More recently, there has been interest in electric-field-induced instabilities in microchannels, in part due to the importance of electric-field-driven transport in micro total analytical system (μTAS) devices (see Chen *et al.* 2005; Ozen *et al.* 2006; Posner & Santiago 2006). Much of the recent work has focused on EK instabilities (EKIs) in microscale channels which use miscible, high-ionic-conductivity electrolyte solutions in which ion diffusion is important. EK instabilities are distinguished from EHD instabilities by the importance of the smearing of conductivity interfaces by ionic diffusion, the role of electro-osmotic (EO) flow in advection and the conditional instability that depends on the electric field and conductivity gradient magnitude. Baygent & Baldessari (1998) were the first to consider the diffusion of ions in a linear stability analysis and predicted conditionally unstable flows at relatively high electric Rayleigh numbers. Oddy, Santiago & Mikkelsen (2001) showed that EKIs could be used to rapidly mix fluids in microscale channels using AC fields. Lin *et al.* (2004) provided a modified ohmic model that can be applied to the study of EKIs with a symmetric binary electrolyte and explored the instability physics using detailed two-dimensional and three-dimensional numerical simulations. Storey *et al.* (2005) studied EKIs in shallow microchannels and showed that the presence of closer channel walls had a stabilizing effect on the instabilities. Chen *et al.* (2005) observed the formation of coherent, wave-like flow structures at the intersection of a microfluidic T-junction using DC applied fields and presented a linear stability analysis on the governing equations to predict the onset of absolutely unstable and convectively unstable modes of instabilities. Oddy & Santiago (2005) extended the instability analysis in symmetric ion electrolytes of Lin *et al.* (2004), Storey *et al.* (2005) and Chen *et al.* (2005) to asymmetric ion mobility electrolytes and predicted that the instability would be observed at lower applied fields than for symmetric electrolytes. Posner & Santiago (2006) observed EKIs in cross-shaped microchannels and characterized the critical electric fields required for instability as a function of the conductivity ratio and stream widths using quantitative scalar imaging. They developed an electric Rayleigh number scaling relationship and showed that the flow becomes unstable at a local critical electric Rayleigh number of $Ra_{e,l} = 205$ over three orders of magnitude of conductivity ratios and stream widths. In the same paper, Posner and Santiago showed scalar power spectrums that exhibit symmetry breaking, bifurcations and continuous power spectrums consistent with highly chaotic flows. These studies collectively provide a fundamental understanding of EKIs, an identification of key controlling parameters, predictive numerical simulations, a description of the critical conditions required for instability and the observation of nonlinear flow patterns.

Existing EKI studies have thus far focused on instabilities in aqueous solutions with mismatched ionic conductivities due to addition of dissolved salts. In this work, we describe instabilities that occur due to gradients in both electrical conductivity and permittivity due to gradients in the volume fraction of micron-scale (500 nm) polystyrene colloidal suspensions with homogeneous background electrolyte solutions. The presence of charge-stabilized colloids can alter the bulk conductivity and permittivity of the solution to which they are added (see Zukoski & Saville 1985). Trau *et al.* (1995) showed that electric fields can be used to induce deformation in a non-dilute colloidal bolus in dielectric mediums, but to our knowledge, the current work represents the first observation of EKIs of non-dilute colloidal suspensions in aqueous electrolyte solutions. Our work in electrolyte solutions is distinguished from the Trau *et al.* (1995) study of dielectric liquids (castor oil) in that electrolyte solutions are highly polarizable and electrically conductive, and particles dispersed in such electrolytes have definable electric double layers (EDLs). We also distinguish our study of unsteady flows in colloidal dispersions with DC fields from steady AC electrothermal flows, which result from thermally induced gradients of conductivity and permittivity (see Sigurdson, Wang & Meinhart 2005).

Our study of instabilities in colloidal suspensions is conducted in Y-shaped polydimethylsiloxane (PDMS) microchannels with pressure- and electric-field-driven flows. We measure the modification of the bulk solution conductivity and particle mobility as a function of the particle volume fraction and show that the critical electric field required for instability is a function of the particle volume fraction ϕ. We develop a scaling relation for the electric body forces developed in the bulk fluid as a function of the charge density that forms due to a coupling of the conductivity and permittivity gradients with the electric field. We show that these colloidal suspensions become unstable at a critical electric Rayleigh number $Ra_{e,crit} = 1.8 \times 10^5$ over two orders of magnitude of the particle volume fraction ($\phi = 0.0001$–0.025).

The paper is organized as follows: in § 2 we analyse the variations in the critical parameters of our study, viz. electrical conductivity, electrophoretic mobility, electrical permittivity and the dynamic viscosity of colloidal suspensions; in § 3 we describe the flow field conditions and the related physical parameters of our experimental system; in § 4 we derive a scaling relation for the electric Rayleigh number that accounts for the variations in the conductivity and permittivity gradients in the flow; in § 5 we describe our experimental set-up, colloidal chemistry, microfabrication of PDMS devices, imaging system and the techniques used to reduce the raw scalar images; in § 6 we present quantitative results reduced from the scalar images and compare the scaling relation with our experimental results. The paper concludes in § 7 with a summary.

2. Variation of suspension properties

In this section we discuss the modification of the bulk solution properties, namely the electrical conductivity, permittivity, viscosity and density as well as the average particle electrophoretic mobility as a function of the particle volume fraction.

2.1. *Variation of the suspension electrical conductivity*

When a charged particle is added to an aqueous electrolyte solution, the conductivity of the solution can increase or decrease depending upon the concentration of the ions in the background electrolyte. A charged sphere dispersed in an electrolyte forms an EDL whose thickness is characterized by its Debye length λ_d (see Hunter 1981). When an electric field is applied, the mobile ions in the diffuse layer of the EDL electromigrate and generate an ionic surface conductance effect that can modify the net electrical conductivity of the solution. In a low-ionic-strength electrolyte, the ionic conductivity in the EDL is greater than that in the bulk solution so that the surface conductance results in an increase in the effective electrical conductivity of the suspension. In contrast, in high-ionic-strength electrolytes, the effect of surface conductance is not appreciable and the particle displaces a volume of solution containing ions that results in a net decrease in the effective electrical conductivity of the suspension. This effect can be captured by the Dukhin number *Du* (see Dukhin 1993). The Dukhin number, *Du*, is the ratio of the surface conductivity to the bulk conductivity of the solution. Thus, it follows that *Du* is higher for particles dispersed in low-ionic-strength solutions and vice versa. The electrical conductivity modification increases with the particle volume fraction ϕ (see Zukoski & Saville 1985). For a given particle volume fraction ϕ, the bulk conductivity of the suspension increases with decreasing EK radius κa (where κ is the inverse Debye layer thickness $(1/\lambda_d)$ and a is the radius of the particle) due to relatively larger EDLs (see Zukoski & Saville 1985).

When dielectric particles with low surface charge (or low *Du* conditions) are added to an electrolyte, the suspension's effective electrical conductivity decreases with increasing volume fraction. This can be described using Maxwell's mean field theory (see Maxwell 1873) and has also been predicted analytically (see Jeffrey 1973; McKenzie, McPhedran & Derrick 1978; Sangani & Acrivos 1983). Watillon & Stone-Masui (1972) measured the surface conductance of 70 nm and 56 nm monodisperse polystyrene latex spheres with volume fractions ranging from 0.003 to 0.010 in perchloric acid solutions. Following this, Dukhin & Derjaguin (1974) extended Smoluchowski's (1918) seminal analysis of EK theory by deriving a relation for the effective electrical conductivity of a dilute suspension of charged particles assuming low zeta potentials (Debye–Huckel approximation) and thin EDLs, while taking into account the distortion of the electric double layer. Saville (1979) and Obrien (1981) predicted the electrical conductivity of suspensions in a symmetric electrolyte for particles with low zeta potential ζ_p and thin EDLs. Obrien (1983) then extended the symmetric electrolyte assumptions of Saville and Dukhin to a general electrolyte case with the limiting case of thin EDLs, uniform zeta potential and immobile stern layer ions. Zukoski & Saville (1985) experimentally measured the particle electrophoretic mobility and suspension electrical conductivity of two different polystyrene latex spheres as functions of volume fraction ($0 < \phi < 0.025$) and used numerical approximations of the EK theory to calculate the zeta potential of particles from these two different measurements. From their analysis, they observed that the values of zeta potentials obtained by these two measurements were substantially different. They attribute this difference in zeta potentials to the transport processes occurring within the stern layer which is not accounted for by the EK theory. Their results indicate that the effective electric conductivity increases with the addition of particles for $\kappa a < 19.1$ and it decreases for $\kappa a > 26.9$. Zukoski & Saville (1987) also measured the electrophoretic mobility and electrical conductivity in a concentrated homogeneous suspension of human erythrocytes with thin EDL assumptions. They confirmed that the bulk conductivity decreases with volume fraction as long as the surface conductance of the particles is much less than that of the solvent medium as suggested by previous analytical predictions (see Jeffrey 1973; McKenzie *et al.* 1978; Sangani & Acrivos 1983). Levine & Neale (1974) and Levine, Neale & Epstein (1976) were the first to employ the Kuwabara's unit cell model (see Kuwabara 1959) method for predicting the electrophoretic mobility and electrical conductivity of dilute suspensions of particles with low zeta potentials. In recent years, several different groups have obtained numerical and analytical expressions taking into account all possible factors, such as, distortion of the double layer, general electrolyte (see Ohshima 1999, 2000), particle–particle interactions (see Johnson & Davis 1999), EDL polarization (see Lee, Chih & Hsu 2001; Keh & Hsu 2002), thick double layers (see Kozak & Davis 1989; Ding & Keh 2001; Carrique, Arroyo & Delgado 2002), overlapping EDLs (see Carrique *et al.* 2003*b*) and dynamic stern layer models (see Voegtli & Zukoski 1991; Carrique, Arroyo & Delgado 2001). There are relatively few experimental studies that measure the electrical conductivity modification of colloidal suspensions and inspite of all the theoretical formulations that have been developed so far, there is no accurate method to predict the variation of electric conductivity of suspensions with volume fraction of particles with thick EDLs, $\kappa a < 1$ (see Ding & Keh 2001).

2.2. *Variation of suspension permittivity*

Electrical permittivity describes a material's ability to polarize in response to an externally applied electric field. Permittivity is a function of the frequency $\varepsilon^*(\omega)$ (F m^{-1}) of the externally applied field, as given by the relation $\varepsilon^*(\omega)=\varepsilon_r^*(\omega)\varepsilon_0$, where $\varepsilon^*{}_r(\omega)$ denotes the complex dielectric constant of the medium and ε_o is the permittivity of free space. The value of the permittivity of a medium at zero frequency (DC) is called its static permittivity or simply the dielectric constant of the medium ε_{rm}. The addition of charged particles to an aqueous solution changes the permittivity of the medium in which they are dispersed. When dealing with a heterogeneous suspension of particles, the electrical permittivity is defined as the value of a sample of homogeneous material that has the same resistance and capacitance as those of the suspension. Many methods have been adopted by researchers to study the frequency dependence of permittivity of colloidal suspensions (see Gregory & Clarke 2005; Ahualli *et al.* 2006). Dielectric spectroscopy (sometimes called low-frequency dielectric dispersion) is one of the most common methods used to study the frequency dependence of the complex permittivity of a suspension in the frequency range of 0.1 kHz to 1 MHz (see Rosen & Saville 1991; Hollingsworth & Saville 2004). However, in the current work, we are primarily interested in the variation of the static permittivity of the particle suspensions. Gregory & Clarke (2005) developed a shielded micrometre-driven, parallel-plate admittance cell device for measuring the permittivity of liquids in the frequency range of 0.1–1 mHz and 5°–50°C temperature range. The permittivity in this case was obtained by measuring the capacitance of the cell filled with the homogeneous liquid sample. They suggested in their paper that such methods are suited only for measuring the capacitances of homogeneous sample liquids due to the problems of fringing fields and stray capacitances that may be associated with heterogeneous samples such as particle suspensions.

The most widely known mechanism of dielectric dispersion that describes the polarization of a heterogeneous material is the Maxwell–Wagner (MW) relation. O'Konski (1960) extended the MW theory to account for the surface conductance effects of particles. Bonincontro, Cametti & Biasio (1980) included the effect of space charge distribution around the dispersed particles which had not been captured by the MW theory by inclusion of a correction factor that is applicable over a wide range of κa and permittivity ratios $\varepsilon_p/\varepsilon_m$. They suggested that correction factors need to be applied to the MW theory to predict the static dielectric constants of suspensions under conditions of small $\kappa a \leqslant 10$ and higher permittivity ratios, $\varepsilon_p/\varepsilon_m \geqslant 1$. Carrique and colleagues (2003*a*) developed a theory for the variations in the static permittivity of suspensions with volume fractions up to 50%, using Kuwabara's cell model. Their theory accounts for the interparticle interactions and overlapping EDLs and suggests that the dielectric constant of the suspension is a function of κa and particle zeta potential (see Carrique *et al.* 2003*a*). They show that the static dielectric constant of the suspension $\varepsilon_{rs}(0)$ as a function of volume fraction typically has a maximum and then decreases contrary to the monotonic decrease predicted by the Maxwell–Wagner–O'Konski relation. In § 6.5, we use Carrique's model to predict the relative importance of the permittivity in the instability as a function of the particle volume fraction and the background solution concentration (see Carrique *et al.* 2003*a*).

To our best knowledge, there is no published data with measurements of the variation in the static permittivity of polystyrene particle suspensions in aqueous solutions as a function of the volume fraction. Dielectric spectroscopy, admittance cell measurement techniques have difficulties measuring the static permittivity, in part due to interference by electrode polarization (see Kijlstra, Vanleeuwen & Lyklema 1993; Tirado *et al.* 2000; Gregory & Clarke 2005; Ahualli *et al.* 2006) and also due to their applicability to heterogeneous samples.

2.3. *Variation of particle electrophoretic mobility*

The electrophoretic mobility μ of a charged particle is often expressed in terms of the particle zeta potential ζ_p by Henry's relation. The particle zeta potential varies with the ionic strength and pH of the background electrolyte (see Kirby & Hasselbrink 2004*a,b*) as well as the particle volume fraction of the suspension (see Hunter 1981). Huckel (1924) first developed an expression for the electrophoretic mobility of a particle in an electric field as a function of the zeta potential of the particle, the fluid permittivity and viscosity of thick EDLs. Henry (1931) extended this theory to consider arbitrary EDL thicknesses and showed that the mobility expression translates to the Smoluchowski's (1918) and Huckel's (1924) equations at thin and thick EDL conditions respectively. In their theories, Henry and Huckel assumed that the EDL is undistorted and unpolarized and that the dispersed particles have low zeta potentials. Overbeek (1950) and Booth (1950) considered distortion of the EDL for moderate values of κa ($0.2 < \kappa a < 50$). Wiersema, Loeb & Overbeek (1996) accounted for the relaxation effects of the EDL with the assumptions of no interparticle interactions, immobile ions in the stern layer, low zeta potential and unpolarized EDL.

The above work (Wiersema, Loeb & Overbeek 1996) primarily focused on the mobility of a single particle in an infinite medium. In a colloidal suspension there are many particles that result in the modification of the mobility due to interparticle interactions. Levine & Neale (1974) were the first to account for the effects of interaction between spherical particles in a colloidal suspension. Approximate analytical expressions for the electrophoretic mobility of dilute suspensions of colloidal spheres in symmetric electrolytes were obtained by Ohshima, Healy & White (1983), which matched well with the numerical simulations of Obrien and White (1978). Several other researchers have also used the dynamic stern layer model of Zukoski & Saville (1985, 1986) to model the variation of electrophoretic mobility with the volume fraction of particles (see Mangelsdorf & White 1990; Kijlstra *et al.* 1992; Arroyo *et al.* 1999; Carrique *et al.* 2001).

The variation of electrophoretic mobility with volume fraction has been measured in concentrated suspensions of homogeneous (see Zukoski & Saville 1987) and heterogeneous (see Zukoski & Saville 1989) erythrocyte suspensions. They showed that the mobility ratio varies as $\mu/\mu_o = (1 - k\phi)$, where k is a constant between 0.97 and 1.15 and μ_o represents the mobility at infinite suspension dilution. More recently, Perez & Lemaire (2004) measured the electrophoretic mobility of poly(methyl methacrylate) (PMMA) particles dispersed in liquid hydrocarbons and showed that the experimental theory of mobility ratio put forward by Zukoski & Saville (1987, 1989) is also applicable to particles in non-aqueous mediums. We also performed experiments to characterize the variation of the average electrophoretic mobility of the polystyrene particles with volume fraction using micron-scale particle image velocimetry (μPIV) technique. The set-up, procedure and results from these measurements are given in § 5.2 of this paper.

2.4. *Variation of solution viscosity and density*

The bulk viscosity is also modified with the colloidal volume fraction. Numerous experimental and theoretical investigations have been carried out to relate the viscosity of colloidal suspensions with the volume fraction of particles (see Guth & Gold 1938; Simha 1940; Vand 1948; Mooney 1951; Krieger & Dougherty 1959; Batchelor 1977; de Kruif *et al.* 1986). Here, we use a maximum volume fraction of $\phi = 0.025$ which remains dispersed in the medium and is distinct from colloidal gels and glasses that can result in non-Newtonian shear thickening and thinning (see Russel, Saville & Schowalter 1989; Franosch *et al.* 1997; Fabbian *et al.* 1999; Larson 1999; Fuchs & Cates 2002). One of the first relations of suspension viscosity with the volume fraction was proposed by Einstein (1906). He suggested that for a collection of hard spherical particles whose radii are larger than those of the solvent and assuming no slip at the solid–liquid boundary, creep flow and no particle hydrodynamic interaction, the dynamic viscosity of the suspension η_s is given by the relation $\eta_s/\eta_m = (1 + 2.5\phi)$, where η_m denotes the dynamic viscosity of the solvent medium. Einstein's relation has been extensively subjected to experimental verification and proven to be accurate within a few percent for $\phi \leqslant 0.01$. For higher volume fractions of spherical particles, a number of extensions to Einstein's equations have been proposed. These relations are discussed in detail by Lyklema (2005). These relations give results similar to Einstein's and predict that the dynamic viscosity of our suspension increases by about 6.7 %–7 % in the range of volume fractions $\phi = 0 - 0.025$ used in the experiments. Similarly, the density of the polystyrene particles is nearly equivalent to the density of the aqueous electrolyte $\rho_p/\rho_m \sim 1.05$, and hence we may assume that the density of the solution does not change appreciably within the range of volume fractions used in our study. We do not expect viscous fingering instabilities will develop in our flows due to density and viscosity differences in a gravitational flow field, as the variation in these parameters are not large enough to cause any instabilities in our experiments (see Saffman & Taylor 1958; Homsy 1987).

As will be discussed in § 4 and § 6.4, variations in the dynamic viscosity and density do not play a significant role in the development of EKIs, and we also show that our simple scaling model matches well with our experimental results over two orders of magnitude of the suspension volume fraction and three orders of magnitude of the applied electric field.

3. Description of the flow conditions

In this work we study EKIs due to gradients in the volume fraction of suspended particles in aqueous electrolytes. In this section, we describe the flow conditions of the study. Figure 1 shows a schematic of the Y-shaped microchannel fabricated using soft lithography of PDMS. The schematic shows (*a*) the stable base state and (*b*) the unstable flow created due to the electric field applied transverse to the colloid volume fraction gradient. Combined pressure and electroosmotic driven flows of

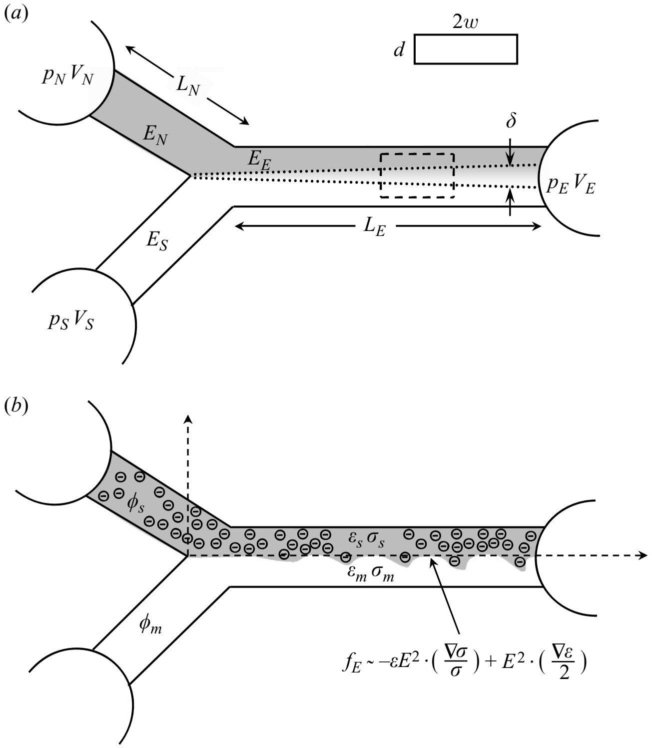

FIGURE 1. Schematic describing the flow conditions at (*a*) stable base state and (*b*) unstable EK flow of particle suspensions in a Y-shaped PDMS microchannel. Buffered aqueous and buffered particle suspensions flow from the south (bottom) and north (top) wells respectively towards the intersection and then flow along the x-axis (streamwise direction) towards the east (right) well. The buffered stream from the south well has no particles ($\phi_m = 0$), ionic conductivity σ_m and electrical permittivity ε_m, and the particle stream from the north well has a particle volume fraction ϕ_s, ionic conductivity σ_s and electrical permittivity ε_s. At the interface of these two streams, there exists a diffusion layer of thickness δ across which the gradients in particle volume fraction, electrical conductivity and permittivity occur. The channels have a half-width w, depth d and lengths L_n. The solution conductivity and permittivity vary with the local particle volume fraction. Applied electric fields couple with the conductivity and permittivity gradients to generate electric body forces that destabilize the flow.

buffered aqueous and buffered aqueous particle suspensions respectively flow from the south (bottom left) and the north (top left) wells and flow away from the Y-intersection along the x-axis (streamwise direction) towards the east (right) well. The buffered aqueous solution used in this case for both the particle and buffer streams is comprised of 0.1 mM concentrations of phosphate buffer. The suspension stream is only distinguished from the buffered stream by the addition of the fluorescent and non-fluorescent polystyrene particles. Since both streams are aqueous, they are fully miscible and form a diffuse interface. The minimum value of the Peclet number in these flows (based on the diffusivity of the particles) is 3.85×10^6 which results in a sharp but miscible interface of the fluorescent particle and buffer streams when the flow is stable. The buffered stream from the south well has no particles $\phi_m = 0$, ionic conductivity σ_m, and electrical permittivity ε_m. The particle stream from the north well has a solution identical to that of the south well with the addition of a particle volume fraction ϕ_s, which results in a solution ionic conductivity σ_s and electrical permittivity ε_s. At the interface of these two streams, there exists a diffusion layer of thickness δ (shown by dotted lines in figure 1) across which the gradients in conductivity and permittivity occur. Here the subscripts m, s denote the medium and the suspension, respectively. The dashed-line box in figure 1(*a*) shows the imaging region of interest which is approximately 1 mm long and 0.2 mm wide.

In our initial experiments, we found that unstable flow structures were rapidly advected downstream due to electro-osmosis- and pressure-driven flows. These flow structures grow exponentially in space but with smaller growth rates near the critical field required for instability (see Posner & Santiago 2006). In order to capture the critical conditions required for onset of instability, we conducted measurements in the east channel 5.5 mm away from the channel Y-intersection, so that they will have adequate time and space to grow and be detected.

The flow velocity in each channel depends on the local electric field E_n, the EO mobility (which is a function of the ionic concentration and the pH of the electrolyte) and both imposed and internally generated pressure gradients. We apply potentials V_N, V_S and V_E to the north, south and east wells respectively such that $V_N = V_S$ and $V_N > \mathrm{V}_E$. PDMS has a negative zeta potential in our buffers (see Kirby & Hasselbrink 2004*a*), and the EO flow will be towards the east well. The particle also has a negative zeta potential (driving it towards the north well) which is greater than that of the channel wall, resulting in a net EK particle motion from the east towards the north well. To force the particles out of the north well and down the east channel, we impose a constant pressure-driven flow rate Q using a dual-syringe pump.

EK flows with gradients in particle volume fractions become unstable when the distortion of the particle stream interface due to internally generated electroviscous velocity occurs faster than the dispersion of this interface due to diffusion of the particles. Figure 1(*b*) shows the schematic of an unstable EK flow. Applied electric fields couple with conductivity and permittivity gradients in the flow to generate electric body forces that renders the flow unstable above a certain critical electric field. Here, we define the quantities E_a, β and γ as

$$E_a \equiv \frac{V_N - V_E}{L_N + L_E}, \tag{3.1}$$

$$\beta \equiv \frac{\varepsilon_{rs}}{\varepsilon_{rm}}, \tag{3.2}$$

$$\gamma \equiv \frac{\sigma_s}{\sigma_m}. \tag{3.3}$$

4. Derivation of the electric Rayleigh number for instability

In this section, we derive a scaling relation for the electric Rayleigh number that accounts for the electric body forces as a function of the conductivity and permittivity gradients in the flow. We start off with a modified Ohmic model of Lin *et al.* (2004) which consists of equations for the conservation for mass with constant density (4.1); conservation of momentum with constant viscosity and density and an electric body force term f_E (4.2); Gauss' Law (4.3); and two convective diffusion equations for the charge density (4.4) and electrical conductivity (4.5):

$$\nabla \cdot \boldsymbol{v} = 0, \tag{4.1}$$

$$Re\left(\frac{\mathrm{D}\boldsymbol{v}}{\mathrm{D}t}\right) = -\nabla p + \nabla^2 \boldsymbol{v} - f_E, \tag{4.2}$$

$$\nabla \cdot (\varepsilon \boldsymbol{E}) = \rho_e, \tag{4.3}$$

$$\nabla \cdot (\sigma \boldsymbol{E}) = 0, \tag{4.4}$$

$$\frac{\partial \sigma}{\partial t} + \boldsymbol{v} \cdot \nabla \sigma = \frac{1}{Ra_e} \nabla^2 \sigma. \tag{4.5}$$

The non-dimensional ionic conductivity and the charge density are defined as

$$\sigma \equiv \frac{F^2(\Lambda_+ C_+ z_+^2 + \Lambda_- C_- z_-^2)}{\sigma_0}, \tag{4.6}$$

$$\rho_e \equiv \frac{F(C_+ z_+ - C_- z_-)}{\varepsilon E_a / w}, \tag{4.7}$$

where F is the Faraday constant; z is the valence number; and Λ is the mobility of ions. The convective diffusion equation for the charge density (4.4) is simply a conservation equation for the electromigration current in the system.

The modified Ohmic model used here is primarily distinguished from the system of equations used by Melcher for EHD (Melcher & Taylor 1969) flows by the inclusion of the diffusive term in the equation for conservation of conductivity (4.5) which was first suggested by the work of Baygents & Baldessari (1998). Baygents & Baldessari (1998) found that molecular diffusion had an important stabilizing effect and is responsible for the existence of a threshold or ‘critical’ Rayleigh number below which their flow was stable.

The related non-dimensional parameters are the Reynolds number,

$$Re = \frac{\rho_0 U_{ev} d}{\eta_m}, \tag{4.8}$$

where ρ_0 and η_m are the medium density and viscosity, and the electric Rayleigh number,

$$Ra_e = \frac{U_{ev} \delta}{D_{eff}}. \tag{4.9}$$

In this case, the appropriate scaling for the diffusivity is that of the particles, in contrast to the ionic diffusivity, since the conductivity and permittivity fields are coupled with the particle distribution. The diffusivity of the particles is given by the Stokes–Einstein equation as

$$D_{eff} = \frac{kT}{6\pi \eta_m a}, \tag{4.10}$$

where a is the particle radius; k is the Boltzmann’s constant; and T is the temperature in Kelvin. Here δ is the diffusion length scale over which the particle volume fraction, electrical conductivity and permittivity gradients occur. The diffusion term does not appear in the final expression for the electric Rayleigh number as it did in previous work (see Posner & Santiago 2006). The electroviscous velocity U_{ev} results from a balance of the viscous and electric body forces in the momentum equation (4.2) and is given as

$$U_{ev} = \frac{f_E d^2}{\eta_m}. \tag{4.11}$$

This is similar to the electroviscous velocity used in the previous work except that here it scales with the entire body forces, not just the electrostatic force $\rho_e E$ (see Baygents & Baldessari 1998; Chen *et al.* 2005; Posner & Santiago 2006). The electric body forces are also due to the gradients in permittivity which contribute to a polarization force that is folded into the electric body force equation. A general expression for the electric body force per unit volume on a liquid is given by the relation (see Stratton 1941)

$$\boldsymbol{f}_E = \rho_e \boldsymbol{E} - \frac{1}{2}\boldsymbol{E}^2 \nabla \varepsilon + \frac{1}{2}\nabla \left(\rho_s \frac{\partial \varepsilon}{\partial \rho_s} \boldsymbol{E}^2 \right). \tag{4.12}$$

The first term is an electrostatic force due to the electric field acting on the net charge density ρ_e in the fluid. Usually in EK flows of aqueous solutions for lab-on-a-chip applications, the net charge is typically considered to be limited to a thin EDL that surrounds solid–liquid and immiscible liquid–liquid interfaces. However, recent reports on EK instabilities have shown that a net charge density can also develop within the bulk fluid, outside the thin EDL at the interface of two liquids with different conductivities (see Lin *et al.* 2004; Chen *et al.* 2005; Oddy & Santiago 2005; Posner & Santiago 2006). The second term is a polarization force due to electric fields coupled with gradients in permittivity, while the third term denotes the body force that may develop due to density differences that may occur due to the deformations of the dielectric, i.e. suspension. Assuming that the particles are hard, rigid spheres, that the fluid is incompressible and that the particle has nearly the density of the background solution ($\rho_p/\rho_m \sim 1.05$), the last term in (4.12) can be assumed to be negligible and is hence neglected.

The key to the scaling analysis is the charge density per unit volume ρ_e described in (4.3). The charge density forms in the bulk regions of flow in which permittivity or conductivity gradient exists and couples with the applied field to generate electrostatic forces in the bulk liquid. From Gauss' Law (4.3), we can write

$$\rho_e = \varepsilon \nabla \cdot \boldsymbol{E} + \boldsymbol{E} \cdot \nabla \varepsilon. \tag{4.13}$$

From (4.4), the conservation equation for current can be written as

$$\nabla \cdot \boldsymbol{E} = -\boldsymbol{E} \cdot \frac{\nabla \sigma}{\sigma}. \tag{4.14}$$

Now (4.13) can be rewritten as

$$\rho_e = -\varepsilon \boldsymbol{E} \cdot \frac{\nabla \sigma}{\sigma} + \boldsymbol{E} \cdot \nabla \varepsilon. \tag{4.15}$$

Following Chen *et al.* (2005) we perform asymptotic expansion of the charge density equation for each variable with the form $f = f_0 + \xi f'$, where the subscript 0 denotes the base state; the prime denotes the perturbation; ξ is a smallness parameter; and terms of the order ξ^2 are dropped as higher order terms. Figure 2(*a*) shows the base state, and figure 2(*b,c*) shows the perturbation states for the flow in consideration. Assuming electroneutrality for the base state (as shown in figure 2*a*) such that $\rho_{e0} \sim \varepsilon_0 \boldsymbol{E}_0 \cdot (\nabla \sigma_0 / \sigma_0) + \boldsymbol{E}_0 \cdot \nabla \varepsilon_0$ is zero (gradients perpendicular to electric fields), the perturbation charge density is given by the relation

$$\rho_e' \sim -\varepsilon \boldsymbol{E}_0 \cdot \frac{\nabla \sigma'}{\sigma_0} - \varepsilon \boldsymbol{E}' \cdot \frac{\nabla \sigma_0}{\sigma_0} + \boldsymbol{E}_0 \cdot \nabla \varepsilon' + \boldsymbol{E}' \cdot \nabla \varepsilon_0. \tag{4.16}$$

In the above equation, we can consider the perturbation charge density arising due to the following four components: (i) the gradient of the conductivity perturbation in the direction of the base electric field; (ii) the electric field perturbation in the direction of the base conductivity gradient; (iii) the gradient of the permittivity perturbation in the direction of the base electric field; and (iv) the electric perturbation in the

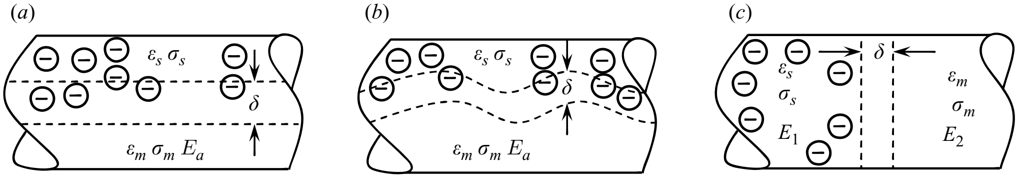

FIGURE 2. Schematic of the east channel for (*a*) stable base state of flow with an axially applied electric field, E_a, and (*b*) unstable state with a charge accumulation ρ_e at the interface of the two streams due to the gradients in the conductivity and permittivity. (*c*) Worst case scenario wherein the conductivity and permittivity gradients are collinear with the applied electric field (similar to that of the Melcher & Taylor 1976 model). The flow and the electric fields are from the left to the right. Conservation of the electromigration current yields $2E_a\gamma\ /(\gamma\ +1)$ on the high-conductivity side and $2E_a/(\gamma\ +1)$ on the lower conductivity side. The electric field in the worst case perturbed state shown in (*c*) is $(E_1\ -E_a) = E_a(\gamma\ -1)/(\gamma\ +1)$.

direction of the permittivity gradient. We now follow Chen *et al.* (2005) who scaled the charge density due to conductivity gradients with the perturbation electric field gradient $\varepsilon \boldsymbol{E}' \cdot \nabla\sigma_0/\sigma_0$ because it represents the strongest possible dependence on gradients of conductivity and the resultant variations in the electric field. To scale the perturbation electric field, we again consider the strongest perturbed conductivity field, which results in a largest value for electric field perturbation and therefore the highest net charge density as shown in figure 2(*c*). If we treat the two electrolyte solutions as resistors in series and assume that half the channel is made up of a low-conductivity solution and the other half of high-conductivity solution, the resistances of these solutions can be expressed as $L/(2\sigma_1 A)$, $L/(2\sigma_2 A)$. With an applied field of E_a we get the following equation for the total current flux through the system as a function of applied field:

$$i = \frac{2E_a\sigma_1\sigma_2}{\sigma_1 + \sigma_2}. \tag{4.17}$$

Conserving the electromigration current in the system, $\nabla \cdot (\sigma E) = 0$, we can determine the electric field in each solution as

$$E_1 = \frac{2E_a\gamma}{\gamma + 1}, \tag{4.18}$$

$$E_2 = \frac{2E_a}{\gamma + 1}, \tag{4.19}$$

where γ is the conductivity ratio σ_s/σ_m. We neglect the diffusive and advective currents because of high-conductivity solutions and thin EDLs (see Probstein 1994). The perturbation field is the local field minus the applied field $E' = E_1 - E_a$ given as

$$E' = E_a\frac{\gamma - 1}{\gamma + 1}. \tag{4.20}$$

The base state conductivity gradient may be scaled as

$$\frac{\nabla\sigma_0}{\sigma_0} \sim \left(\frac{(\sigma_s - \sigma_m)/2\delta}{(\sigma_s + \sigma_m)/2}\right) \sim \left(\frac{1}{\delta}\frac{\gamma - 1}{\gamma + 1}\right). \tag{4.21}$$

The permittivity gradient coupled with an electric field also contributes to the charge density as shown in the third and fourth terms of (4.16). Scaling the charge density with the fourth term would result in $\boldsymbol{E}'.\nabla\varepsilon_0 \sim E_a(\gamma - 1)/(\gamma + 1)\nabla\varepsilon$. However, this scaling suggests that a conductivity gradient is required for charge to be generated when an electric field is coupled with a permittivity gradient. Since this is not physically relevant to our flows in which both the conductivity and permittivity gradients can independently generate a charge density, scaling with the gradient of the perturbation term $\boldsymbol{E}_0 \cdot \nabla \varepsilon'$ is more appropriate. Thus, we have

$$\rho_e' \sim -\varepsilon \boldsymbol{E}' \cdot \frac{\nabla \sigma_0}{\sigma_0} + \boldsymbol{E}_0 \cdot \nabla \varepsilon'. \tag{4.22}$$

The above scaling method allows for the development of charge density in a flow field in the presence of permittivity gradients alone when the conductivity field is uniform, $\nabla \sigma_0 \sim 0$. The gradient of the permittivity perturbation term can now be scaled as

$$\nabla \varepsilon' \sim \nabla \varepsilon \sim \frac{\varepsilon_m - \varepsilon_s}{\delta} = \frac{\varepsilon_m (1 - \varepsilon_s/\varepsilon_m)}{\delta} = \frac{\varepsilon_m}{\delta}(1-\beta). \tag{4.23}$$

The perturbation charge density now scales as

$$\rho_e' \sim -\frac{\varepsilon_m}{\delta}\left(\frac{\gamma - 1}{\gamma + 1}\right)^2 E_a + \frac{\varepsilon_m}{\delta}(1-\beta)E_a. \tag{4.24}$$

The electric body force term, f_E is then expressed as

$$f_E \sim \frac{\varepsilon_m}{\delta}\left(\frac{\gamma - 1}{\gamma + 1}\right)^2 E_a^2 + \frac{\varepsilon_m}{2\delta}(1-\beta)E_a^2, \tag{4.25}$$

where the final term for f_E includes contributions from both electrostatic and polarization forces. Combining (4.9), (4.10), (4.11) and (4.25), the expression for the electric Rayleigh number becomes

$$Ra_e \sim \varepsilon_m d^2 E_a^2 \frac{6\pi a}{kT}\left[\left(\frac{\gamma - 1}{\gamma + 1}\right)^2 - \left(\frac{1-\beta}{2}\right)\right]. \tag{4.26}$$

Table 1 lists the constants used in (4.26). Here, the electric Rayleigh number definition does not depend on the local diffusion thickness (since it is cancelled by the δ^{-1} term in the body force term of (4.25)) or the fluid viscosity (since it is cancelled by the viscosity in the particle diffusivity equation (4.11)). This scaling suggests that gradients in either the conductivity (left term in square brackets) or permittivity (right term) can alter the electric Rayleigh number and drive the instability. The above formulation for the electric Rayleigh number will be used in our subsequent analysis, and it will be shown in § 6.5 that this describes the trends of instability onset observed in our experiments.

It is to be noted here that the above equations for the conservation of mass (4.1) and momentum (4.2) are not applicable to colloidal systems such as gels and glasses which exhibit the properties of viscoelasticity, shear thickening and thinning. As described earlier in § 2.4, we predict that the density will not vary more than 0.2 %, and the viscosity will not vary more than 7 %. Although these modifications may alter the local flow patterns, we argue that these modifications do not drive the instability or alter the physics that govern the onset of instability. In § 6.5, we show good agreement between the above scaling relation and experimental results, which suggests that the modification in the density and viscosity are not critical to predicting the onset of instability in this particle volume fraction range.

5. Experimental methodology

In this section, we describe our experimental set-up, imaging system, electronics, colloidal chemistry, microchannel fabrication and the processing of raw scalar images.

Symbol	Description	Value
ε_{rm}	Buffer relative dielectric constant	78.55 at 25° C
ε_{rp}	Particle relative dielectric constant	2.4
η_m	Water dynamic viscosity	1.0×10^{-3} kg m^{-1}s^{-1}
ς_p	Particle zeta potential	−80 mV
ρ_m	Water density	1.0×10^3 kg m^{-3}
ρ_p	Particle density	1.05×10^3 kg m^{-3}
D_{eff}	Stokes–Einstein particle diffusivity	4.365×10^{-13} m^2 s^{-1}
K	Boltzmann's constant	1.38×10^{-23} JK^{-1}
D	Channel depth	3.0×10^{-5} m

TABLE 1. Values of experimental parameters and fundamental constants used in the study. The depth of the PDMS microchannel was measured by using a profilometer (KLA-Tencor Corporation, San Jose, CA, USA).

5.1. *Scalar imaging: experimental set-up and image analysis*

We obtained instantaneous scalar images of fluorescent particle streams using epifluorescence microscopy and charge-coupled device (CCD) camera imaging. Figure 3 shows the experimental set-up. Experiments were performed in Y-shaped PDMS microchannels fabricated using soft lithography. The channels have a rectangular cross-section with a half-width of $w = 100\,\mu$m, depth $d = 30\,\mu$m and total length of 15 mm ($L_N = 5$ mm; $L_E = 10$ mm). Pressure-driven flow was maintained by a dual-syringe pump (KDS200P, KD Scientific, Holliston, MA, USA). The syringes were connected to the chip using Tygon tubes (ID 0.02″ OD 0.06″ VWR, Brisbane, CA, USA) which were interfaced to the PDMS reservoirs via stainless steel tubes (0.025 OD × 0.017 ID, 0.5″ length, New England Small Tube, Litchfield, NH, USA). Electric potentials were applied using platinum electrodes (Omega Engineering Inc., Stamford, CT, USA) inserted into the Tygon tubes approximately 5 mm above the top chip surface. We expect that there is negligible drop in the electrical potential between the wire insertion point and the channel entrance, since the area of the tube is about four orders of magnitude larger than the cross-sectional area of the microchannel, and the potential drop in the tube should be less than 0.1 V.

The electric potentials were applied and synchronized to the CCD image acquisitions, using a high voltage sequencer (HVS448 6000D, Labsmith, Livermore, CA, USA). For typical currents and duration as observed in our experiments (at the highest possible electric field, $E_a \sim 1000$ V cm^{-1}), we do not observe significant electrolysis bubble generation. If small bubbles do form, they remain within the tygon tubing that is used to deliver the pressure-driven flows into the microfluidic chips. An epifluorescent microscope (Nikon TE2000, Japan) with a 10×, NA = 0.30 objective (Nikon, Japan), metal halide illumination (EXFO X-Cite 120, Ontario, Canada) and epifluorescent filter cube (excitation at 540 nm, emission at 625 nm; Chroma, Rockingham, VT, USA) were used to image the flow. Images were recorded on a back-illuminated, Peltier-cooled, 16 bit CCD camera with on-chip gain (Cascade IIb Photometrics, Tucson, AZ, USA) fitted with a 0.63× demagnifier.

We then normalize each image of scalar concentration for systematic errors with the equation

$$C_j(x, y) = \frac{I_j(x, y)_{raw} - \overline{I(x, y)_{dark}}}{\overline{I(x, y)_{flat}} - \overline{I(x, y)_{dark}}}, \tag{5.1}$$

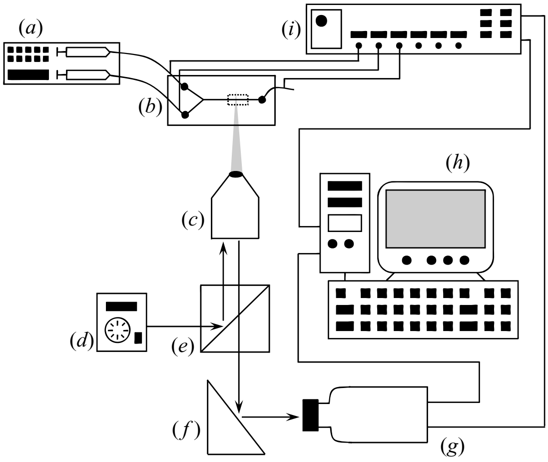

FIGURE 3. Experimental set-up of epifluorescence microscopy used for imaging the flows with the following system components: (*a*) syringe pump; (*b*) PDMS microfluidic device; (*c*) objective; (*d*) metal halide bulb; (*e*) epifluorescence filter cube; (*f*) reflector; (*g*) CCD camera with a 0.63 demagnifier; (*h*) computer; (*i*). high-voltage sequencer.

where

$$\overline{I(x,y)} = \frac{\sum_{j=1}^{n} I_j(x,y)}{n-1}. \tag{5.2}$$

Here the instantaneous image index is j, and the subscripts *raw*, *dark* and *flat* denote the raw, dark-field and flat-field images respectively. The flat-field images are recorded with the entire channel filled with the particle suspension and help to correct for non-uniform illumination and variations in the channel height, i.e. depth averaging. The dark-field images are recorded with the channels filled with the aqueous buffer and correct for external light scattered off channel walls and not chromatically filtered, fluorescence from wall-adsorbed particles and sensor dark noise. We record 100 frames of dark- and flat-fields before and after each experiment, respectively.

5.2. *Electrophoretic mobility measurements: experimental set-up and analysis*

The electrophoretic mobility of particles is typically a function of the suspension volume fraction (see Zukoski & Saville 1987, 1989). Measurements of the average electrophoretic mobility of the particles as a function of volume fraction were also performed. The measurements were conducted in a 200 μm square glass capillary channel suspended across an acrylic frame with fluid reservoirs at its ends. The acrylic capillary support was fabricated using a laser ablation system (Universal Laser, Scottsdale, AZ, USA). We suppressed the EO flow in the capillary by coating the inner walls of the channel using polyethylene oxide (PEO) (see Preisler & Yeung 1996). Suppressing the EO flow in the channel enabled for direct measurement of the average electrophoretic mobility of the particle without the effect of EO flow. Electric potentials were then applied through platinum electrodes dipped into the liquid reservoirs containing particle suspensions. After filling the liquid reservoirs and before conducting the measurements, we waited for the height of the liquid in the reservoirs to equalize. The absence of particle motion signified equalization in the pressure head across the fluid reservoirs. Digital images of the electrophoretic motion of particles in the channel were recorded with a CCD camera (Cascade IIb, Photometrics, Tucson, AZ, USA). To obtain precise times between images, the camera was triggered by a frequency generator (Agilent Technologies, USA). We used standard cross-correlation PIV algorithms with ensemble averaging in correlation space to obtain the velocity fields (see Wereley *et al.* 1998). Interrogation window of 128 pixels × 8 pixels with a 50 % overlap was used and then area averaged to obtain the average value for the particle electrophoretic velocity. Velocity was measured for six different values of electric fields ($E = 20$ V cm^{-1}–150 V cm^{-1}) at each of the five different values of volume fraction of particles ($\phi = 0$–0.02). The particle mobility $\mu = U_{ep}/E$ at each volume fraction was then extracted as the slope of a least squares linear fit with $R^2 \geqslant 0.99$ from the plot of the electrophoretic velocity as a function of the electric field. From these experiments, it was found that the mobility ratio approximately obeyed the expression $(1 - k\phi)$ as proposed by Zukoski & Saville (1987, 1989). The value of the constant k observed from our experiments was about two orders of magnitude lower than that observed by Zukoski & Saville (1987, 1989), indicating that there was very little or no variations in the electrophoretic mobility of particles with volume fraction in our buffers. The value of the constant k increases with decreasing ionic strength of the background electrolyte, which suggests that the decrease in the mobility ratio is more dramatic at lower ionic strength electrolytes because of thicker EDLs. Further details of these measurements are included in Navaneetham (2007).

5.3. *Colloid and solution chemistry*

For the instability experiments, the background aqueous buffer solution used was 0.1 mM phosphate buffer prepared by the titration of monosodium phosphate (NaH_2PO_4) conjugate acid with disodium hydrogen phosphate (Na_2HPO_4) conjugate base (Sigma Aldrich, St. Louis, MO, USA). The pH and conductivity of the buffer solution were respectively 6.0 and 29.4 μS cm^{-1} as measured using a combination pH/conductivity meter (Corning, NY, USA). This background solution was chosen as it provided for large modifications in the bulk fluid conductivity due to the addition of the particles and also buffered changes in the pH due to electrolytic reactions at the electrodes. The buffered solutions were filtered prior to making the particle suspensions, using a 450 nm syringe filter (Millipore, Billerica, MA, USA). Negatively charged, 500 nm polystyrene particles (Duke Scientific Inc, Fremont, CA, USA) were used in this work. The fluorescent polystyrene microspheres had respective excitation and emission wavelengths of 542 nm and 612 nm. We define the volume fraction ϕ of particles as

$$\phi = \frac{n \cdot \frac{4}{3}\pi a^3}{V}, \tag{5.3}$$

where n is the number of particles; a is the particle radius; and V is the total volume of the solution. The particle suspensions consisted of both fluorescent and non-fluorescent polystyrene particles. The volume fraction of fluorescent spheres was maintained constant at $\phi = 0.0003$, and the volume fraction of non-fluorescent particles was varied from $\phi = 0.0022$ to $\phi = 0.0247$ in all of our experiments. We measure the conductivity of the resultant particle solutions by measuring the ohmic currents across a glass capillary filled with the colloidal suspension at seven different applied voltages (see Navaneetham 2007). Care was taken not to use electric fields that resulted in significant Joule heating. The solution conductivity was then determined using the relation $\sigma = IL/AV$, where A, L are the cross-sectional area and length of the capillary, respectively. The ratio of I/V was measured as the least squares linear fit of the applied voltage versus the Ohmic current with R-squared values greater than 0.99. These measurements were also compared with the conductivity measurements from a standard conductivity meter (Corning, NY, USA) and were found to be in very good agreement. The solution conductivities reported here were measured using the capillary method.

Average zeta potential of both the fluorescent and non-fluorescent particles at infinite dilutions were also measured separately using a dynamic light scattering (DLS) system (PSS Nicomp, Santa Barbara, CA, USA) and found out to be equivalent to $\zeta_p = -80$ mV. Zeta potentials of particles dispersed in phosphate buffers at four different concentrations were also measured and are provided in the Appendix.

5.4. *Microfabrication of PDMS devices*

Soft lithography of PDMS was used to fabricate the Y-shaped microchannels. Details of this process can be found elsewhere (see Duffy *et al.* 1998), but we have included a brief procedure specific to this work. Masks were produced on transparent mylar sheets using a high resolution (20 000–50 000 dpi) printing system (Fineline Imaging, Colorado Springs, CO, USA). SU-8 (negative photoresist) patterned on a 4″ silicon wafer served as the master for soft lithography. The surface of the master was silanized with trichloro methyl silane (TCMS) vapor for about 30 minutes. PDMS (Dow Corning Corporation, Midland, MI, USA) in a 10:1 polymer: fixing agent ratio was poured over the master, degassed at low pressure in a dessicator and baked at 80° C in a convection oven for 60 minutes. The resultant structures were then exposed to oxygen plasma (Tegal Plasmaline Asher, Rocklin, CA, USA) at a power of 200 W and 400 mJ pressure for 60 seconds.

5.5. *Experimental conditions*

For the instability experiments, we recorded data for six values of particle volume fractions $\phi = 0.0025$, 0.005, 0.008, 0.011, 0.018, 0.025 all dispersed in a 0.1 mM concentration of phosphate buffer, four values of imposed pressure-driven flow rates $Q = 50\,\mu\text{L hr}^{-1}$, $100\,\mu\text{L hr}^{-1}$, $150\,\mu\text{L hr}^{-1}$ and $200\,\mu\text{L hr}^{-1}$ and nominally applied fields E_a spanning over three decades from 0 to 1200 V cm^{-1}. For each case, we ramped the field E_a from 0 V cm^{-1} to a maximum field in steps of 13.3 V cm^{-1} (20 V each step). The maximum allowed field was set by the flow rate and difference in mobility of the particles and the channel walls. Since the electrophoretic mobility of the particles is larger than that of the channel, the net EK motion in the particle stream is in the direction of positive electrode (north). At large electric fields, the velocity of the particles exceeds the local velocity due to the pressure-driven and EO flows in the channel, and the particles do not enter the east channel. The use of positively charged particles would have avoided the usage of external pressure-driven flows, but fluorescently labelled, neutrally buoyant, positively charged particles are not readily available and adsorb to the channel walls.

We record 100 frames at each applied field with 100×512 pixels at 70 frames per second with 2 ms exposure time. In addition to these systematic sets of experiments, additional experiments were also performed to ensure repeatability across different conditions and microfluidic devices. Calibration experiments were also performed prior to the reported instability experiments to ensure that the steady flow rates could be maintained from the syringe pump over the duration of the experiment.

Before the start of each experiment, the chip microchannels were flushed thoroughly with deionized (DI) water for about 10 minutes and 0.1 mM phosphate buffer solution

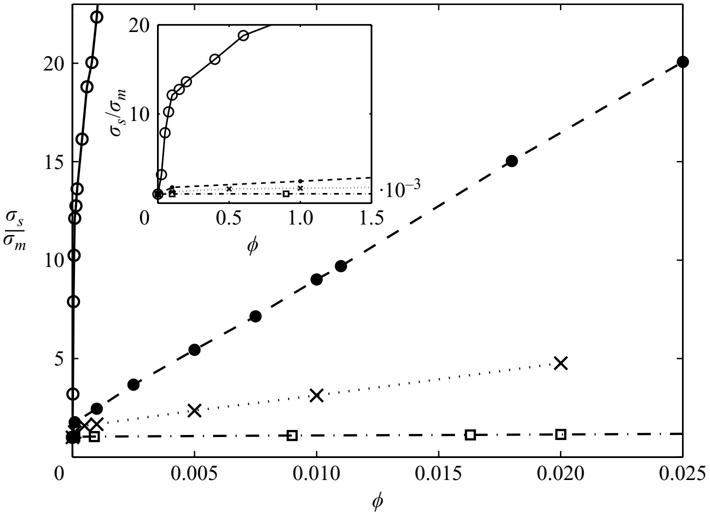

FIGURE 4. Variation of the electrical conductivity with volume fraction of negatively charged 500 nm polystyrene particles. Experimental data points are shown for particles in four different electrolytes: –○–DI water ($\kappa a \sim 1$); – – ● – –0.1 mM phosphate buffer ($\kappa a \sim 8$); -×-1 mM phosphate buffer ($\kappa a \sim 25$); - □ - -10 mM phosphate buffer ($\kappa a \sim 80$). The inset shows the variation of the conductivity at lower volume fractions. The electrical conductivity increases with particle volume fractions. The slope of the curve increases with decreasing background ionic strength.

for an additional 10 minutes. All the digital images were taken at a constant distance 5.5 mm east from the channel intersection. Images were acquired after a 3 second delay of changing the potential, allowing the flow to reach a steady condition. The elapsed time for each experiment was approximately 9 minutes. All the experiments were performed with a constantly imposed pressure-driven flow of 100 μL hr^{-1} unless otherwise noted. To elucidate the dependence on flow rate, additional experiments were conducted with varying flow rate and a constant volume fraction of $\phi = 0.011$.

6. Results and discussions

In this section, we first present the measured variation of electrical conductivity with the volume fraction of particles. We then describe the steady base state conditions and qualitative analysis of the unstable flow fields obtained by the reduction of scalar images. We discuss our technique for determining the critical electric field required for unstable flows and show how the critical electric field varies with the volume fraction ϕ and imposed pressure-driven flow rate Q. The measured critical field is compared with the simple scaling analysis, which shows that the flow becomes unstable at a critical electric Rayleigh number of $Ra_e = 1.8 \times 10^5$ within the range of volume fractions in our study.

6.1. *Measurement of non-dilute suspension conductivity*

It is well known that the EDL streaming current surrounding colloidal particles can contribute to a modification in the suspension's conductivity as reviewed in § 2.1. We measure the variation of our colloidal suspension's conductivity with volume fraction at three different values of buffer ionic strengths. Figure 4 shows the values of solution conductivity as a function of the particle volume fraction ϕ for DI water and 0.1, 1 and 10 mM phosphate buffer. The resulting EK radii κa are approximately 1, 8, 25 and 80 for the DI, 0.1, 1 and 10 mM phosphate buffers, respectively. The conductivity for each solution is normalized by the conductivity of the base electrolyte at zero volume fraction. The inset of figure 4 shows the conductivity at small volume fractions. For volume fractions greater than $\phi > 0.0001$, the conductivity increases linearly with volume fraction. As expected, the slopes of the curves increase with decreasing background electrolyte (and EK radius κa) concentration due to increase in *Du*, which indicates the appreciable role of surface conductance around the particle relative to the conductance of the background solution. At higher ionic strengths (and κa), the relative thickness of the Debye length shrinks (see Probstein 1994), and the magnitude of the zeta potential of the particles decreases (see Kirby & Hasselbrink 2004) which results in a decreased surface conductance effect. The zeta potential of our particles at infinite dilution are listed in the Appendix. In the case of DI water, there is an initially steep slope for volume fractions below $\phi < 0.0001$ which is observed in the experiments. This curvature is due to the electric-field-induced distortion of the EDL and surface conductance effects of the relatively thick and isolated EDL of each particle in low-ionic-strength DI solution (see Carrique *et al.* 2003). The scaling relation presented in equation (4.26) requires a relation for the suspension conductivity ratio γ as a function of the volume fraction. We obtain this by making a least squares linear fit of the 0.1 mM buffer data, and it is given by the relation

$$\frac{\sigma_s}{\sigma_m} = \gamma = 780\phi + 1, \tag{6.1}$$

with an R-squared value of 0.9940.

To confirm that the variation of the electrical conductivity of the suspension was due to the particles and not packaged background salt or surfactants, we performed additional experiments. A particle solution with a volume fraction of $\phi = 0.01$ dispersed in a 1 mM, pH 7 phosphate buffer with an electrical conductivity of 301.1 μS cm^{-1} was taken as a test solution. We then spun this solution down in a centrifuge at 8600 R.P.M. for about 50 minutes. The extracted supernatant fluid contained no particles, and its electrical conductivity was measured to be approximately equivalent to that of the base solution within experimental uncertainties. A similar experiment was also performed with the 0.1 mM phosphate buffer, and consistent results were obtained. Dissolved salts and surfactants cannot be separated using a centrifuge, so the spun solution still contained them. The results of these experiments thus indicated that the variation in the suspension conductivity was clearly due to the particle EDL streaming current as predicted and measured by various researchers as reviewed in § 2.1.

6.2. *Stable base state and unstable flows*

In this section, we first describe the conditions of the stable base state flow and the qualitative features of the instabilities developed. Figure 5 shows representative scalar images of the flow recorded at the Y-intersection with $Q = 300\,\mu$L hr^{-1}, $\phi = 0.011$, at various applied electric fields. Figure 5(*a*) shows instantaneous representative scalar fields of the steady base state at 0 V cm^{-1} in which the particle and the buffer streams flow steadily from the north and south wells respectively towards the east well. As we increase the electric field to around 1000 V cm^{-1}, the particles begin to aggregate as shown in figure 5(*b*). These aggregates are visualized as regions of bright intensity. Electric field-induced-particle aggregation has been observed in electrorheological flows with conductive particles in insulating liquids (see Trau *et al.* 1995). We have

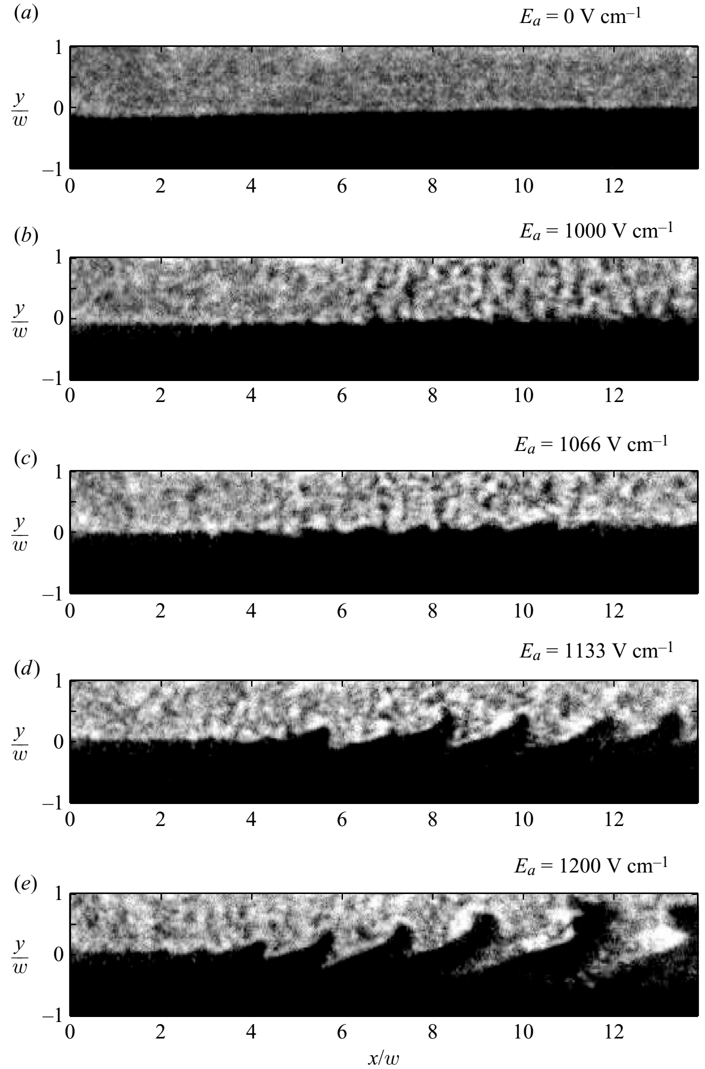

FIGURE 5. Instantaneous scalar images $C_j(x,y)$ of EK flows with non-dilute particle suspensions. The bottom buffered stream is 0.1 mM phosphate buffer, and the top stream is 0.1 mM phosphate buffer with particle volume fraction $\phi = 0.011$ of polystyrene particles. Flows are in 200 micron wide PDMS microchannels with pressure-driven flow rate $Q = 300$ μl hr^{-1} and applied fields E_a noted above each image. The images are taken at the Y-intersection of the east channel. (*a*) At low electric field the flow is stable. (*b*) At 1000 V cm^{-1}, the particles aggregate and form clusters as observed by the high-fluorescence-intensity regions. At 1066 V cm^{-1}, the flow becomes moderately unstable as can be seen by the wrinkling of the particle interface. As the field increases further, coherent wavelike structures are observed. The instabilities grow as they advect downstream along the east channel.

observed particle aggregation at fields below critical electric fields for instability, with particle sizes ranging from 500 nm to 10 μm and with and without volume fraction gradients. At larger fields, $E_a = 1066$ V cm^{-1}, the flow becomes marginally unstable as denoted by the wrinkling of the particle stream interface at $x/w > 6$ as shown in figure 5(*c*). As we further increase the electric field to $E_a = 1133$ V cm^{-1}, the disturbances grow rapidly, forming coherent wavelike structures that grow in magnitude at $x/w > 6$ as shown in figure 5(*d*). Upon further increasing the electric field to $E_a = 1200$ V cm^{-1}, the perturbations increase in magnitude and originate further upstream at $x/w \sim 4$. The perturbation magnitude grows along the length of channel, x/w, and the particle and buffer streams appear to be well mixed down the channel.

Figure 6 shows instantaneous scalar images recorded at a distance of 5.5 mm from the intersection with a reduced pressure-driven flow velocity of $Q = 100\,\mu\mathrm{L\ hr}^{-1}$ and $\phi = 0.025$ at various electric fields. The qualitative features of the flow are similar to those for the higher flow rate case; however we see that the perturbations are larger for a given electric field because the volume fraction is larger, and the advective velocity is lower, and we observe the perturbations further downstream. The magnitude of the scalar perturbations depends on the external pressure-driven flow velocity Q. At a given electric field, the magnitude of the perturbation increases with decreasing flow rate. The pressure-driven flow advects the instabilities down the east channel, while the instability temporal growth rate is set by the applied field. We use this downstream, low-flow-rate condition for determining the critical electric field because it provides the most precise measure. At high flow rates, the perturbations are advected downstream before they can grow large enough to be observed. At lower flow rates, the net EK motion of the particles (the EO flow minus the electrophoretic velocity) can exceed the pressure-driven flow, resulting in the migration of the particles to the north well. For this reason, all the determination of the critical electric field, E_c, was conducted with a constantly imposed pressure-driven flow rate of $Q = 100\,\mu\mathrm{L\,hr}^{-1}$. In § 6.5, we present the critical electric field at $Q = 100\,\mu\mathrm{L\ hr}^{-1}$, and in § 6.6, we explain how the pressure-driven flow influences the instabilities.

Separate experiments were also carried out with the addition of 10 µM concentration of fluorescein dye (with an excitation and emission wavelengths of 498 nm and 525 nm respectively) to visualize the flow independent of the particles. These experiments showed that the flow and not just the motion of the particles is unstable.

6.3. *Interpretation and analysis of scalar images*

In this section, we briefly discuss our method of analysing the quantitative scalar images. The average scalar field is calculated as

$$\overline{C(x, y)} = \frac{\sum_{j=1}^{n} C_j(x, y)}{(n-1)}, \tag{6.2}$$

where n is the number of images. The mean square perturbation energy is calculated as

$$\overline{C'(x, y)^2} = \frac{\sum_{j=1}^{n} C'_j(x, y)^2}{(n-1)}, \tag{6.3}$$

where the scalar perturbation is $C'_j(x, y) = C_j(x, y) - \overline{C(x, y)}$. Figure 7 shows the mean square scalar perturbation fields for $\phi = 0.025$, $Q = 100\,\mu\mathrm{L\ hr}^{-1}$. Figure 7(*a*) shows the stable base state perturbation field corresponding to zero applied electric field. Although the applied field is zero, there still is finite perturbation energy throughout the particle-laden region due to the random distribution of fluorescent particles. The variation in fluorescent intensities coupled with the pressure-driven flow results in a finite value of perturbation energy. Figure 7(*b*) is stable but shows a slight increase in the perturbation energy due to particle aggregation. Figure 7(*c*) shows marginally unstable flow at regions near the interface $(y/w) \sim 0$ in which the conductivity and permittivity gradients are the largest. As we increase the applied electric field E_a, the perturbations grow in magnitude and extend further into the particle and non-particle

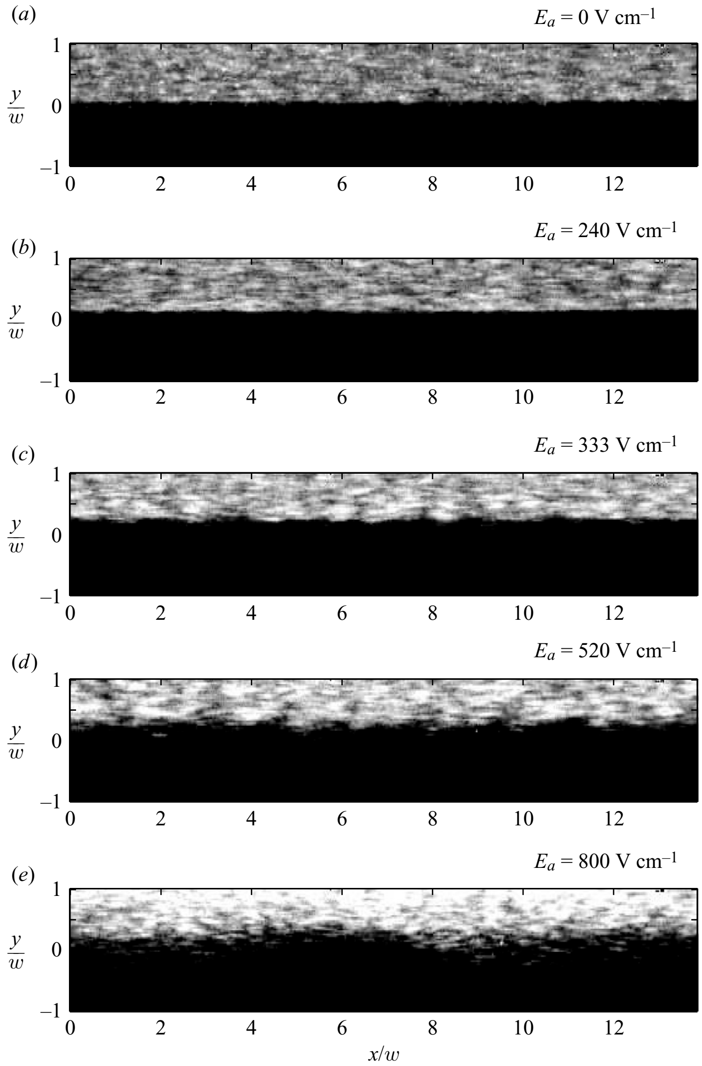

FIGURE 6. Instantaneous scalar images $C_j(x,y)$ of EK flows with non-dilute particle suspensions. The bottom buffered stream is 0.1 mM phosphate buffer, and the top stream is 0.1 mM phosphate buffer with particle volume fraction $\phi = 0.025$ of polystyrene particles. Flows are in 200 micron wide PDMS microchannels with pressure-driven flow rate $Q = 100 \mu l\, hr^{-1}$ and applied fields E_a noted above each image. Images are taken in the east channel 5.5 mm downstream of the Y-intersection. These images are representative of the conditions and region of interest that was used to determine the critical electric field. (*a*) At low electric field the flow is stable. (*b*) At moderate field 240 V cm^{-1} the particles aggregate and form clusters of high fluorescence intensity. At 333 V cm$^{-1,}$ the flow becomes moderately unstable as can be seen by the wrinkling of the particle interface. As the field increases further, sinuous structures are observed.

streams on either side of the interface as shown in figure 7(*d, e*). We found that the magnitude of these mean square scalar perturbation values increases with decreasing pressure-driven flow rate, *Q*. In § 6.6, we show how the perturbation energy and critical electric field required for instability depend on the pressure-driven flow rate.

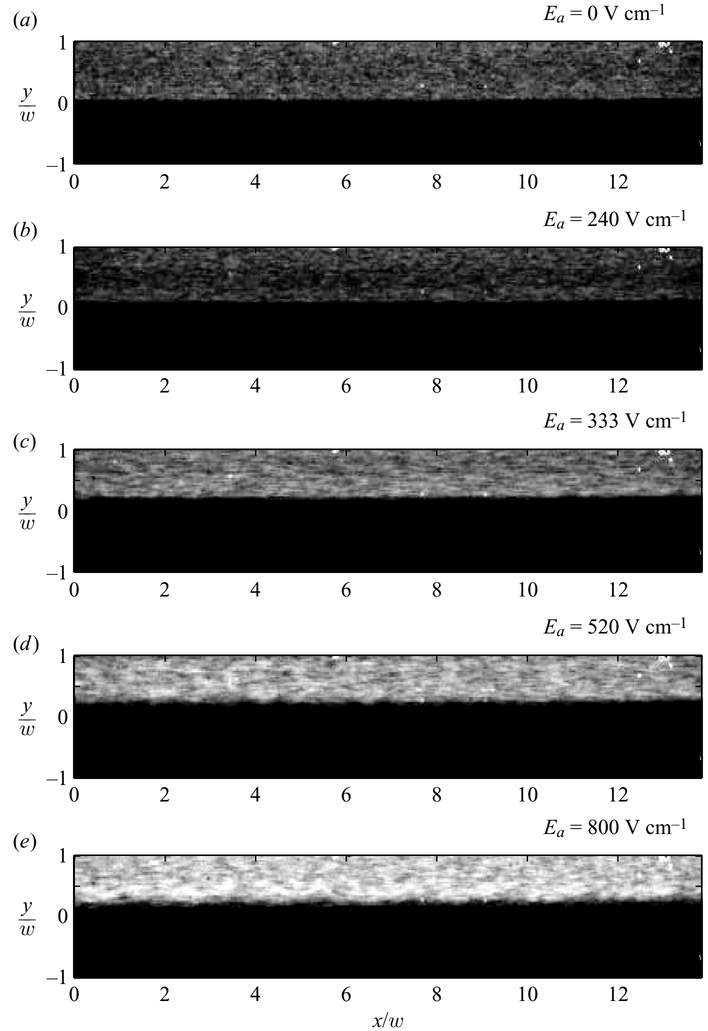

FIGURE 7. Scalar perturbation energy fields $\overline{C'(x,y)^2}$ of EKIs in east channel at 5.5 mm downstream of the Y-intersection with $\phi = 0.025$ and pressure-driven flow of $Q = 100\,\mu\text{l hr}^{-1}$ (experimental conditions of figure 6). When the flow becomes unstable, $E = 333$ V cm^{-1}, localized regions of high perturbation energy are observed along the region of interface in which the conductivity and permittivity gradients are the maximum. As the field is increased further, the instabilities grow, resulting in larger magnitude perturbation energies. The perturbation fields are used to determine the critical field required for onset of the instability.

6.4. *Perturbation surface plots*

Figure 8 shows x-area-averaged surface maps of scalar perturbation versus the applied field E_a and transverse coordinate y/w for a pressure-driven flow velocity of $Q = 100\,\mu\text{L hr}^{-1}$ and volume fractions of (*a*) $\phi = 0.005$, (*b*) $\phi = 0.008$, (*c*) $\phi = 0.018$ and (*d*) $\phi = 0.025$. These plots are obtained by averaging the scalar perturbation fields $\overline{C'(x,y)^2}$ in the streamwise x direction, resulting in an area-averaged perturbation energy $\langle \overline{C'(x,y)^2} \rangle_x$, where the brackets denote the spatial average, and the subscript x denotes the direction. At low electric fields, the average perturbation energy in the particle-laden stream $y/w > 0$ is at a base value. The perturbation energy remains

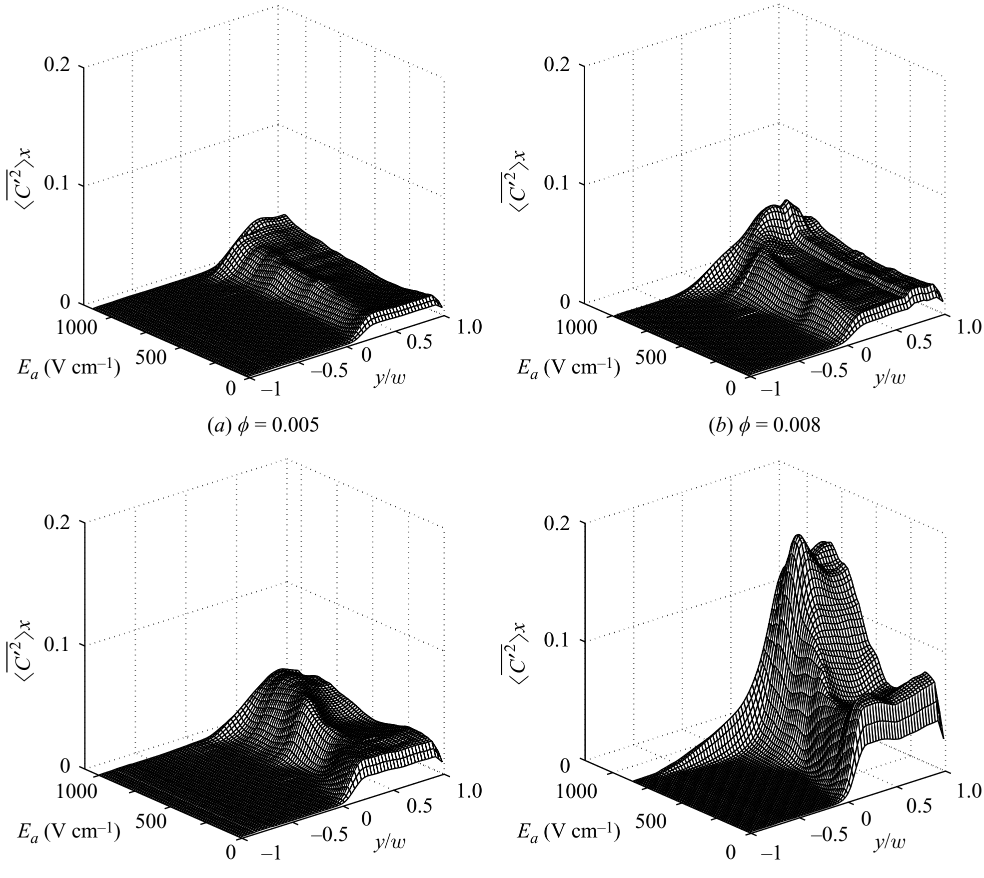

(a) $\phi = 0.005$ (b) $\phi = 0.008$

(c) $\phi = 0.018$ (d) $\phi = 0.025$

FIGURE 8. Surface maps of x-area-averaged scalar perturbation energies $\langle\overline{C'^2}\rangle_x$ as functions of nominally applied field E_a and transverse channel dimension y/w. Maps are shown for $Q = 100\,\mu\mathrm{l}\ \mathrm{hr}^{-1}$ and particle volume fractions of (a) $\phi = 0.005$, (b) $\phi = 0.008$, (c) $\phi = 0.018$ and (d) $\phi = 0.025$. The perturbation energy increases from a base value at the critical applied electric field E_c. The critical electric field decreases with increasing volume fraction. The base perturbation energy varies with volume fraction because of secondary scattering of non-fluorescent particles. The increase in perturbation energy is most pronounced at the particle interface, $y/w = 0$. At higher electric field the perturbation energy moves into the buffered stream as shown in (b) at $\sim$900 V cm^{-1}.

at this base level until the critical applied electric field E_c is reached, at which the perturbation energy starts to increases from its base value. This behaviour is distinctly visible at the interface of the two streams ($y/w \sim 0$), where the conductivity and permittivity gradients are the largest. For example in figure 8(d) the maximum value of the perturbation curve increases monotonically from its base value of $\sim$0.06 at $E_a \sim 300$ V cm^{-1} until 850 V cm^{-1} at which it starts to decrease. This decrease in the perturbation energy at higher applied electric fields is primarily due to the reduction in the number of fluorescent particles in the region of interest, when the particles retract into the north well due to the net EK velocity exceeding the pressure-driven and EO flow velocities. Note that the position of the maximum perturbation energy shifts to $y/w > 0$ at higher electric fields because the particle/buffer interface shifts due to the electrophoretic drift of the particles. As the volume fraction increases the

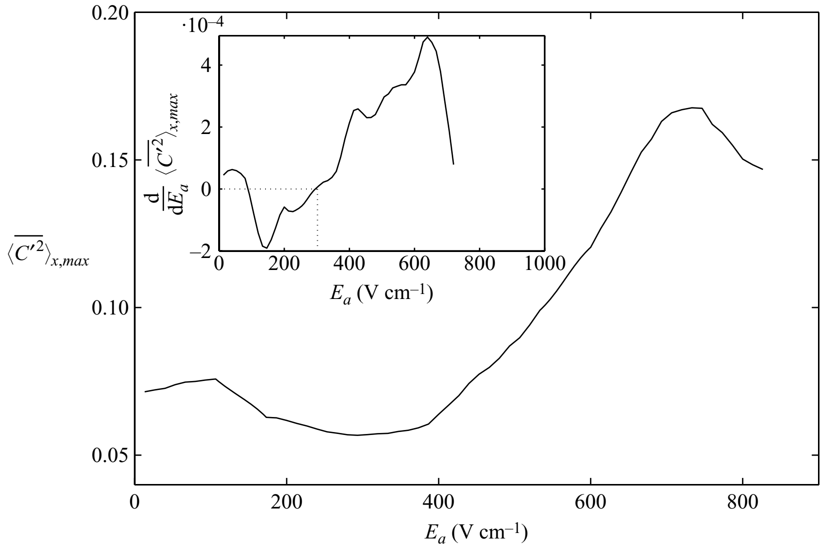

FIGURE 9. Plot of the maximum x-area-averaged scalar perturbation energy $\langle\overline{C'^2}\rangle_{x,max}$ as a function of applied electric field E_a for $\phi = 0.025$ and $Q = 100\,\mu\text{L hr}^{-1}$. The critical electric field is defined as the field in which the maximum perturbation energy in the system starts to increase monotonically ($E_c = 302.5$ V cm^{-1}). The inset shows the derivative of the maximum perturbation energy curve with respect to the electric field. The critical electric field is defined as the field in which the perturbation energy starts to increase monotonically and is simply equal to $d(\langle\overline{C'^2}\rangle_{x,max})/dE_a = 0$ which is denoted with a dashed line.

maximum perturbation increases, and the critical electric field decreases. We expect this behaviour because the conductivity and permittivity gradients in the flow increase with the volume fraction. The next section will discuss the quantitative determination of the critical electric field for instability as a function of the volume fraction ϕ.

6.5. *Variation of critical electric field with particle volume fraction*

To determine the critical field required for instability, we start by calculating the maximum value of the averaged scalar perturbation energy$\langle\overline{C'^2}\rangle_{x,\,max}$ for each electric field as shown in figure 9 for $\phi = 0.025$, $Q = 100\,\mu\text{L hr}^{-1}$. The initial decrease in the maximum perturbation energy curve is due to the onset of the particle's electrophoretic drift in the reverse flow direction. The perturbation energy increases when the flow becomes unstable. We define the critical electric field E_c as the value of the applied field at which the maximum value of the scalar perturbation energy starts to increase from its base value and increases monotonically as a function of the applied field. In practice, we determine the critical field by calculating its derivative in respect to the electric field $\mathrm{d}\langle\overline{C'^2}\rangle_{x,\,max}/\mathrm{d}E_a$ as shown in the inset of figure 9. The critical electric field is simply defined as the electric field at which the value of $\mathrm{d}\langle\overline{C'^2}\rangle_{x,\,max}/\mathrm{d}E_a$ reaches zero as denoted by the dashed lines.

We spatially average in the streamwise direction to increase the sensitivity of our algorithm for determining the critical electric fields. In our previous EKI work on ionic conductivity gradients we averaged the perturbations in the transverse direction and showed that the instabilities grow exponentially in the axial direction consistent with the perturbation theory (see Posner & Santiago 2006). In this previous work we showed that the exponential growth rate K increased with the applied electric field.

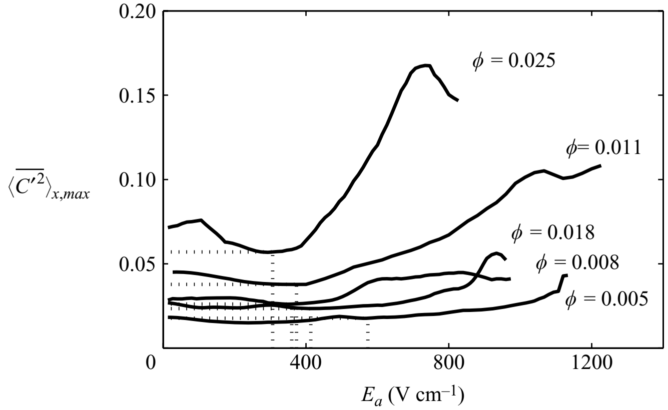

FIGURE 10. Plot of the maximum averaged scalar perturbation energy profiles for $\phi = 0.005$, 0.008, 0.011, 0.018 and 0.025 at a pressure-driven flow velocity of $Q = 100\,\mu$L hr^{-1}. The dashed line denotes the critical electric field for each volume fraction. The perturbation energy increases with the applied electric field above the critical field required for instability. The slope of the perturbation energy increases with volume fraction. The critical electric field is defined as the field in which the perturbation energy begins to increase from its base value. The base perturbation value generally increases with volume fraction because of secondary scattering from non-fluorescent particles.

The colloidal instabilities studied here have smaller exponential growth rates due to the decreased mobility of the charge-carrying species (i.e. the particles), such that no growth in the axial direction is observed for $Q = 100\,\mu$L hr^{-1} over the region of interest. For this reason, averaging the scalar perturbation energies in the streamwise direction reduces noise in the measurement of the maximum scalar perturbations in the flow.

This critical field definition is distinct from our previous definition that is defined as the field in which the magnitude of the area-averaged perturbation energy reaches a value twice that of the base state (see Posner & Santiago 2006). We showed that this arbitrary definition for the critical field is consistent with a change from a zero exponential spatial growth rate to a non-zero one. Our previous definition works well for flows with ionic concentration gradients in which the change in the area-averaged perturbation increases with the nearly infinite slope at the critical field. However, this previous definition for the critical field does not work for suspension instabilities studied here in which the perturbation energy can vary with the electric field for stable base state flows, and there is a gradual increase in the perturbation energy at the critical field. Our current definition is more appropriate for flows with varying base state perturbation energies and can also be applied to the previous work, resulting in consistent results. Figure 10 shows the maximum averaged scalar perturbation energy profiles for $\phi = 0.005$, 0.008, 0.011, 0.018 and 0.025 at a constant flow rate $Q = 100\,\mu$L hr^{-1}.

The base state (low electric field) perturbation energy generally increases with volume fraction. We attribute this variation in base perturbation energies to secondary scattering of non-fluorescent particles and variations in the fluorescent intensity distribution in the particle stream. This effect is independent of the applied field because it is observed even without an applied field. The critical electric field is determined using the method described above and denoted by dashed the lines in figure 10.

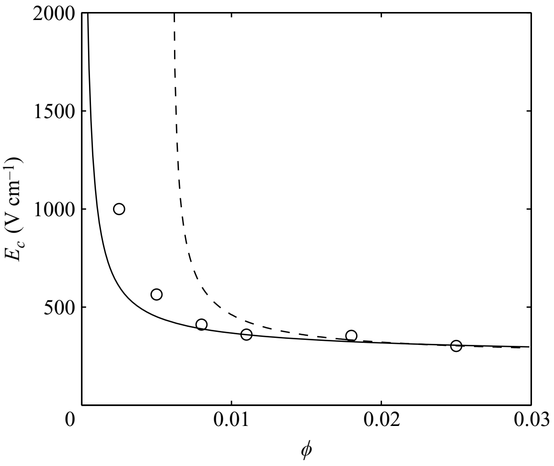

FIGURE 11. Plot of the variation of critical electric field required for the onset of EKIs as function of the particle volume fraction ϕ. The circles in figure 11 indicate experimental results. The solid line and the dashed lines respectively indicate the scaling analysis of (4.26) including and neglecting (with $\beta = 0$) the effects of the permittivity ratio β. The critical field asymptotes to $E \sim 300$ V cm^{-1} for large volume fractions. The critical electric field increases as volume fraction approaches zero. The scaling analysis accounts for modifications in the electrical conductivity and permittivity due to suspension volume fraction. Here we set the critical Rayleigh number value to $Ra_{e,crit} = 1.8 \times 10^5$ and 0.65×10^5 to obtain the solid and dashed lines respectively.

Our methodology for determining the critical electric field is independent of the base state perturbation energy and results in consistent and reproducible results. We have repeated every experimental data point in figure 11 at least two times and found the critical field to always lie between +/—13.3 V cm^{-1}, which is the minimum step size used for increasing the electric field in our experiments. This variation is smaller than the height of the symbols used in figure 11 which represents approximately 50 V cm^{-1}. The uncertainty in the electric field is approximately 3.3 V cm^{-1}.

The critical electric fields extracted from figure 10 are plotted as functions of the volume fraction denoted by open circles in figure 11. The solid and dashed lines are obtained from the scaling analysis presented in § 4. The electric Rayleigh number expression as a function of the experimental parameters and the applied electric field is represented by (4.26). From (4.26), we determine the critical electric field by setting the Rayleigh number equal to the critical value, $Ra_e = Ra_{e,crit}$, setting the electric field equal to the critical value, $E_a = E_c$, in (4.26) and isolating E_c. The relation for the critical electric field E_c is simply obtained from (4.26) as

$$E_c = \sqrt{\frac{kT\,Ra_{e,crit}}{6\pi a d^2 \varepsilon_m \left[\left(\frac{\gamma - 1}{\gamma + 1}\right)^2 - \left(\frac{1-\beta}{2}\right)\right]}}. \tag{6.4}$$

This formulation describes the critical electric field as a function of the fluid properties, particle radius, channel depth, electrical conductivity and permittivity gradients and the critical Rayleigh number. This scaling relation does not predict the Rayleigh number but simply describes the dependence of the critical electric field on the known parameters of the system (a, d, ε, γ, β, T) and the critical electric Rayleigh number. The conductivity ratio γ, described by (6.1), is obtained from a linear fit of all the experimental data points for the electrical conductivity variation of suspensions with volume fraction of particles in 0.1 mM phosphate buffer. The permittivity ratio β as a function of volume fraction is calculated using Carrique's (2003*a*) model. We have chosen this model because it takes into account the interparticle interactions and overlapping EDL effects of concentrated particle suspensions and precisely predicts the suspension dielectric constant variation as a function of both volume fraction and frequency. The model also concurs well with available and existing experimental measurements of dielectric constants of suspensions found in the colloids literature. The permittivity as a function of the volume fraction for several buffer concentrations and zeta potentials is given in the Appendix.

Figure 11 shows good qualitative agreement between the trends predicted by the scaling relation and the quantitative experimental data. The solid line and the dashed lines respectively show the scaling analysis of (6.4), including and neglecting ($\beta = 0$) the effects of the permittivity ratio β. We obtain the electric Rayleigh number at which the flow becomes unstable by fitting the scaling analysis with the experimental data and setting the critical electric Rayleigh number to $Ra_{e,crit} = 1.8 \times 10^5$ and 0.65×10^5 to obtain the solid and the dashed lines respectively. It is to be noted here that the electric Rayleigh number value is an arbitrary quantity that describes the onset of the instability under the electric Rayleigh number defined here. The goal of the scaling analysis and the electric Rayleigh number is to provide qualitative prediction of the variation of the critical electric field with the particle volume fraction. At large volume fractions, the critical electric field asymptotes at about $E_c = 300$ V cm^{-1}. For particle volume fractions, $\phi > 0.008$, the charge accumulation at the interface due to conductivity gradients saturates, and the critical electric field required for instability reaches an asymptote. At volume fractions ϕ less than 0.008 the critical field increases rapidly due to the relatively small conductivity and permittivity gradients. Experiments with volume fractions, $\phi < 0.002$, were also carried out, but the critical electric fields in those experiments required large electric fields that resulted in net EK motion of the particles in the upstream direction, and hence the critical field could not be determined.

Figure 11 suggests that the permittivity plays a significant role in the instability mechanism. To examine this, we plot the ratio of the conductivity $(\gamma - 1/\gamma + 1)^2$ and permittivity gradients $(1\text{-}\beta)/2$ that play a role in the electric Rayleigh number equation (4.26) in figure 12. This ratio describes the relative importance of the conductivity and permittivity gradients in driving the electroviscous velocity that results in unstable flow. In 0.1 mM phosphate buffer, the conductivity contributes nearly six times more than the permittivity at $\phi < 0.01$. At larger volume fractions of the order of $\phi \sim 0.1$, the permittivity contributes nearly a third of the net electroviscous effects. As the ionic strength of the buffers increases (increasing κa) the slope of the conductivity versus the volume fraction curve decreases as shown in figure 4. In 10 mM buffer, the surface conductance of the particles is small compared to buffer conductance (low Du), such that the conductivity is independent of the suspension volume fraction, resulting in ratio much less than unity for $\phi < 0.04$. This suggests that, under some conditions, the permittivity gradients can be the main driving force of the instability. At a volume fraction of $\phi = 0.005$ the permittivity effects in the 0.1 mM case are only 15 % of the conductivity, in contrast to the 10 mM case in which the permittivity effects are 10 times as large as the conductivity effects. At a volume fraction of $\phi = 0.1$ the permittivity effects in the 0.1 mM case account for about 33 % of the conductivity,

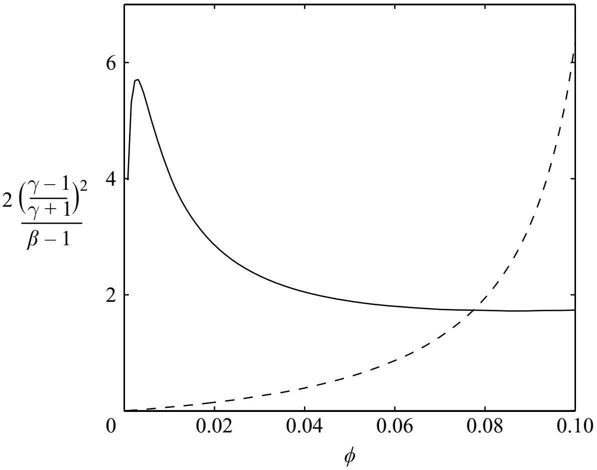

FIGURE 12. Plot of the relative effects of the conductivity and permittivity gradients as functions of volume fraction. This ratio describes the relative importance of the conductivity and permittivity gradients in driving the electroviscous velocity that results in unstable flow. The solid line is for 500 nm polystyrene particles dispersed in 0.1 mM phosphate buffer at pH 6. The dashed line is for the same particle in 10 mM buffer at pH 7. The plot indicates the relative contributions of the conductivity and permittivity gradients to the electric Rayleigh number. In 0.1 mM phosphate buffer, the conductivity contributes nearly six times more than the permittivity for $\phi < 0.01$. At larger volume fractions of the order of $\phi \sim 0.1$, the permittivity contributes nearly a third of the electroviscous velocity. In 10 mM buffer, the surface conductance of the particles is small compared to buffer conductance, resulting in a ratio much less than unity for $\phi < 0.04$. This suggests that, under some conditions, the permittivity gradients can be the main driving force of the instability.

in contrast to the 10 mM case in which the permittivity effects are only 10 % of the conductivity effects.

This decrease in the permittivity effects at higher concentrations of particles in a 10 mM buffer solution is due to a less pronounced change in the static permittivity at these higher volume fractions (see the Appendix for the permittivity values). The permittivity and its role in EKIs is a function of volume fraction ϕ, zeta potential of particles ζ_p, the EK radius κa and the permittivity of the particles ε_p and the medium ε_m. It is to be noted here that the conditions encountered in our experiments do not represent a generic condition for all electrolytes, and particles. Alternate models or experimental data can be used to determine the permittivity ratio β, and the electric Rayleigh number scaling in (4.26) can be used as generic scaling relation for determining the conditions under which the flow will become unstable.

In our previous work, we showed that EKIs with ionic conductivity gradients develop when the electric Rayleigh number reaches 205. Here, we observe a much larger critical Rayleigh number. The high Ra_e is due to low diffusive coefficients for the particles. Here the particles have a Stokes–Einstein diffusivity of $8.58 \times 10^{-13}\,\mathrm{m^2\,s^{-1}}$, where ions have a diffusivity that is four orders of magnitude larger. If we use the diffusivity of the ions namely sodium and hypophosphate ions, in the flow we calculate an electric Rayleigh number of around 250. Although this value is much closer to our previous work (see Posner & Santiago 2006), it does not accurately represent the diffusivity of the conductivity and permittivity fields. Here the conductivity and

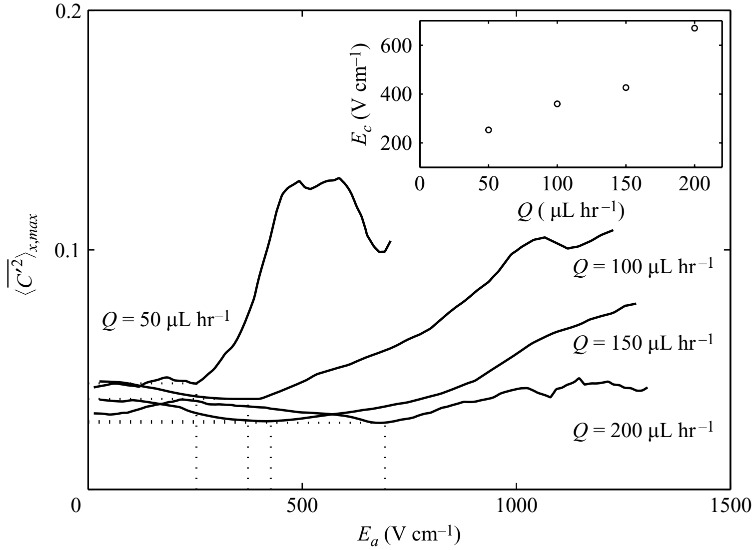

FIGURE 13. Plot of the maximum, x-area-averaged scalar perturbation energies for $\phi = 0.011$ and pressure-driven flow rates $Q = 50$, 100, 150 and 200 μL hr^{-1}. The dashed line shows the perceived critical electric field for each flow rate. The inset shows a plot of the measured critical electric field as a function of the pressure-driven flow rate. The measured critical field increases with the pressure-driven flow rate. The pressure-driven flow advects the instability perturbations downstream which results in a perceived stabilizing effect.

permittivity fields are coupled with the particles, and thus the particle diffusivity is more appropriate than the ionic diffusivity.

6.6. *Influence of pressure-driven flows on EKIs*

Experiments were also performed to ascertain the effect of increasing the imposed pressure-driven flow rate Q. Figure 13 shows a plot of the maximum x-area-averaged scalar perturbation energy profiles for $\phi = 0.011$ and $Q = 50$, 100, 150 and 200 μL hr^{-1}. The inset of figure 13 shows the critical electric field as a function of the flow rate as determined by the method described in the previous section. The inset shows that the field required to register as an instability increases nearly linearly with the imposed pressure-driven flow rate Q. We attribute this measured increase in the critical field to the increase in the advective velocity. The temporal growth rate of the instabilities is a function of the applied field and should not depend on the pressure-driven flow rate. However, as we increase the flow rate, the structures are advected downstream faster and have less time to grow which results in a reduction in the spatial growth rate and scalar perturbation energy at the fixed location at which they are measured. The increased flow rate is a perceived stabilizing effect. It follows that magnitudes of electric fields higher than that of the actual critical electric field are generally required in order to observe detectable perturbations in the system. For this reason, the most accurate measurements of the critical electric field will be obtained with the lowest possible velocity. In the current work, it is not possible to reduce the flow rate below 50 μL hr^{-1} because the net EK velocity will then exceed the pressure-driven flow velocity, resulting in no particles in the east channel. Note that it is possible to observe the onset of instability at the critical electric field, E_c, at various flow rates provided the observation window is moved downstream. However, we were limited in our ability to move the observation window further downstream, as the current location of the observation window in all our experiments is at a distance of 5.5 mm downstream from the Y-intersection along the east channel, and the east channel is only 10 mm.

7. Conclusions

EKIs can occur in flows with colloidal suspensions when there is a coupling of applied electric fields with gradients in particle volume fraction. Particles in suspension can modify the bulk solution electrical conductivity and permittivity. Electric fields couple with the gradients in conductivity and permittivity to generate electric body forces that can render the flow unstable under certain conditions. The flow becomes unstable when the electroviscous stretching and folding of the conductivity and permittivity interfaces exceed the dissipative effects of viscous forces and particle diffusion.

We have presented an experimental investigation of EKIs developed in non-dilute colloidal suspensions. The conductivity and permittivity gradients were generated at the intersection of a Y-shaped PDMS microchannel. We have explored the variations in the critical electric field required for flow instability as a function of colloidal volume fraction and pressure-driven flow rates. The variations in the effective electrical conductivity of a suspension and the average electrophoretic mobility with volume fraction of particles were determined experimentally. We have shown that EKIs in non-dilute colloidal suspensions are characterized by wavelike coherent structures which grow in magnitude as they advect downstream. We used quantitative scalar imaging and showed that the critical electric field required for instability depends upon volume fraction of particles in the suspension. We developed scaling relations for the electric body forces in the bulk fluid as functions of both the conductivity and permittivity gradients in the flow and showed that the flow becomes unstable at a critical electric Rayleigh number $Ra_e = 1.8 \times 10^5$.

EKIs in colloidal suspensions may be important in the EK manipulations of non-dilute colloidal systems such as electrorheological flows, field-induced pattern formations in colloidal dispersions, field-induced layering of colloidal crystals films and electronic chip cooling as well as a host of on-chip EK manipulations of biomolecules for μTAS applications.

The authors thank Professors Angel Delgado and Felix Carrique for their valuable contributions of the prediction of dielectric constant variations with volume fractions. G.N. appreciates the help of Philip M. Wheat and Abhishek Jain with microfabrication of PDMS devices. This work was sponsored by an NSF CAREER Award (J.D.P., grant number CBET-0747917) with William Wendell Schultz as the grant monitor. The authors acknowledge the use of facilities within the Center for Solid-State Electronics Research at Arizona State University.

Appendix. Suspension permittivity as a function of volume fraction

The permittivity of a colloidal suspension generally varies with the particle radius, permittivity, zeta potential and volume fraction, as well as the solution concentration (Debye layer thickness). Here we use Carrique's (2003*a*) model to estimate the permittivity of our 500 nm polystyrene suspensions in various ionic strength phosphate buffers. Table 2 lists the permittivity of polystyrene suspensions for six volume fractions and DI water for background buffer solutions of phosphate buffer. The zeta potential values are measured using dynamic light scattering (DLS) at infinite dilution.

Buffer	Zeta ζ_p	Volume fraction of particles ϕ					
		0.001 %	0.01 %	0.1 %	1 %	3 %	10 %
DI water	−110 mV	78.58	78.83	80.88	92.66	102.96	101.90
0.1 mM	−80 mV	78.59	78.96	82.19	105.09	135.28	165.15
1 mM	−52 mV	78.57	78.69	79.82	87.67	97.51	103.86
10 mM	−33 mV	78.55	78.59	78.90	80.86	82.70	79.94
100 mM	−10 mV	78.55	78.54	78.48	77.73	75.88	68.88

TABLE 2. The permittivity of 500 nm polystyrene suspension in various phosphate buffer solutions. The zeta potentials of the particles ζ_p are measured at infinite dilution by DLS.

REFERENCES

AHUALLI, S., JIMENEZ, M. L., DELGADO, A. V., ARROYO, F. J. & CARRIQUE, F. 2006 Electroacoustic and dielectric dispersion of concentrated colloidal suspensions. *IEEE Trans. Dielec. Elec. Insul.* **13**, 657–663.

ARROYO, F. J., CARRIQUE, F., BELLINI, T. & DELGADO, A. V. 1999 Dielectric dispersion of colloidal suspensions in the presence of stern layer conductance: particle size effects. *J. Colloid Interface Sci.* **210**, 194–199.

BATCHELOR, G. K. 1977 Effect of Brownian-motion on bulk stress in a suspension of spherical-particles. *J. Fluid Mech.* **83**, 97–117.

BAYGENTS, J. & BALDESSARI, F. 1998 Electrohydrodynamic instability in a thin fluid layer with an electrical conductivity gradient. *Phys. Fluids* **10**, 301–311.

BAZANT, M. Z. & SQUIRES, T. M. 2004 Induced-charge electrokinetic phenomena: theory and microfluidic applications. *Phys. Rev. Lett.* **92**, 066101-1 to 066101-4.

BONINCONTRO, A., CAMETTI, C. & BIASIO, A. D. 1980 Effect of volume ion polarisations on Maxwell–Wagner dielectric dispersions. *J. Phys.* D. **13**, 1529–1535.

BOOTH, F. 1950 The cataphoresis of spherical, solid non-conducting particles in a symmetrical electrolyte. *Proc. R. Soc. Lond.* **A 203**, 514.

CARRIQUE, F., ARROYO, F. J. & DELGADO, A. V. 2001 Electrokinetics of concentrated suspensions of spherical colloidal particles: effect of a dynamic stern layer on electrophoresis and DC conductivity. *J. Colloid Interface Sci.* **243**, 351–361.

CARRIQUE, F., ARROYO, F. J. & DELGADO, A. V. 2002 Electrokinetics of concentrated suspensions of spherical colloidal particles with surface conductance, arbitrary zeta potential, and double-layer thickness in static electric fields. *J. Colloid Interface Sci.* **252**, 126–137.

CARRIQUE, F., ARROYO, F. J., JIMENEZ, M. L. & DELGADO, A. V. 2003*a* Dielectric response of concentrated colloidal suspensions. *J. Chem. Phys.* **118**, 1945–1956.

CARRIQUE, F., ARROYO, F. J., JIMENEZ, M. L. & DELGADO, A. V. 2003*b* Influence of double-layer overlap on the electrophoretic mobility and DC conductivity of a concentrated suspension of spherical particles. *J. Phys. Chem. B* **107**, 3199–3206.

CHEN, C. H., LIN, H., LELE, S. K. & SANTIAGO, J. G. 2005 Convective and absolute electrokinetic instability with conductivity gradients. *J. Fluid Mech.* **524**, 263–303.

DE KRUIF, C. G., VAN IERSEL, E. M. F., VRIJ, A. & RUSSEL, W. B. 1986 Hard sphere colloidal dispersions: viscosity as a function of shear rate & volume fraction. *J. Chem. Phys.* **83**, 4717–4725.

DING, J. M. & KEH, H. J. 2001 The electrophoretic mobility and electric conductivity of a concentrated suspension of colloidal spheres with arbitrary double-layer thickness. *J. Colloid Interface Sci.* **236**, 180–193.

DUFFY, D. C., MCDONALD, J. C., SCHUELLER, O. J. A. & WHITESIDES, G. M. 1998 Rapid prototyping of microfluidic systems in poly(dimethylsiloxane). *Analyt. Chem.* **70**, 4974–4984.

DUKHIN, S. & DERJAGUIN, B. V. 1974 *Surface and Colloid Science*. Wiley.

DUKHIN, S. S. 1993 Nonequilibrium electric surface phenomena. *Adv. Colloid Interface Sci.* **44**, 1–134.

ESPIN, M. J., DELGADO, A. V. & REJON, L. 2005 Electrorheologial properties of hematite/silicone oil suspensions under dc fields. *J. Non-Newton. Fluid Mech.* **125**, 1–10.

Fabbian, L., Gotze, W., Sciortino, F., Tartaglia, P. & Thiery, F. 1999 Ideal glass–glass transitions and logarithmic decay of correlations in a simple system. *Phys. Rev. E* **59**, R1347–R1350.

Franosch, T., Fuchs, M., Gotze, W., Mayr, M. R. & Singh, A. P. 1997 Theory for the reorientational dynamics in glass-forming liquids. *Phys. Rev.* E **56**, 5659–5674.

Fuchs, M. & Cates, M. E. 2002 Theory of nonlinear rheology and yielding of dense colloidal suspensions. *Phys. Rev. Lett.* **89**, 248304-1 to 248304-4.

Gregory, A. P. & Clarke, R. N. 2005 Traceable measurements of the static permittivity of dielectric reference liquids over the temperature range 5–50 degrees C. *Meas. Sci. Technol.* **16**, 1506–1516.

Guth, E. & Gold, O. 1938 *Physical Review* **53**, 322.

Hayward, R. C., Saville, D. A. & Aksay, I. A. 2000 Electrophoretic assembly of colloidal crystals with optically tunable micropatterns. *Nature* **404**, 56–59.

Henry, D. C. 1931 The cataphoresis of suspended particles. Part 1. The equation of cataphoresis. *Proc. R. Soc. of Lond.* A **133**, 106.

Hoburg, J. F. & Melcher, J. R. 1976 Internal electrohydrodynamic instability and mixing of fluids with orthogonal field and conductivity gradients. *J. Fluid Mech.* **73**, 333–351.

Hollingsworth, A. D. & Saville, D. A. 2004 Dielectric spectroscopy and electrophoretic mobility measurements interpreted with the standard electrokinetic model. *J. Colloid Interface Sci.* **272**, 235–245.

Homsy, G. M. 1987 Viscous fingering in porous-media. *Ann. Rev. Fluid Mech.* **19**, 271–311.

Huckel, E. 1924 Die Kataphorese der Kugel. *Physik. Z.* **25**, 204.

Hunter, R. J. 1981 *Zeta Potential in Colloid Science*. Academic.

Ikazaki, F., Kawai, A., Uchida, K., Kawakami, T., Edamura, K., Sakurai, K., Anzai, H. & Asako, Y. 1998 Mechanisms of electrorheology: the effect of the dielectric property. *J. Phys.* D **31**, 336–347.

Jang, S. P. & Choi, S. U. S. 2006 Cooling performance of a microchannel heat sink with nanofluids. *Appl. Therm. Engng* **26**, 2457–2463.

Jeffrey, D. J. 1973 Conduction through a random suspension of spheres. *Proc. R. Soc. Lond.* A **335**, 355–367.

Johnson, T. J. & Davis, E. J. 1999 An analysis of electrophoresis of concentrated suspensions of colloidal particles. *J. Colloid Interface Sci.* **215**, 397–408.

Keh, H. J. & Hsu, W. T. 2002 Electric conductivity of a suspension of charged colloidal spheres with thin but polarized double layers. *Colloid Polym. Sci.* **280**, 922–928.

Kijlstra, J., Vanleeuwen, H. P. & Lyklema, J. 1992 Effects of surface conduction on the electrokinetic properties of colloids. *J. Chem. Soc., Faraday Trans.* **88**, 3441–3449.

Kijlstra, J., Vanleeuwen, H. P. & Lyklema, J. 1993 Low-frequency dielectric-relaxation of hematite and silica sols. *Langmuir* **9**, 1625–1633.

Kirby, B. J. & Hasselbrink, E. F. 2004*a* Zeta potential of microfluidic substrates. Part 1. Theory, experimental techniques, and effects on separations. *Electrophoresis* **25**, 187–202.

Kirby, B. J. & Hasselbrink, E. F. 2004*b* Zeta potential of microfluidic substrates. Part 2. Data for polymers. *Electrophoresis* **25**, 187–213.

ozak, M. W. & Davis, E. J. 1989 Electrokinetics of concentrated suspensions and porous-media. Part 2. Moderately thick electrical double-layers. *J. Colloid Interface Sci.* **129**, 166–174.

Krieger, I. M. & Dougherty, T. J. 1959 A mechanism for non-Newtonian flow in suspensions of rigid spheres. *Trans. Soc. Rheol.* **3**, 137.

Kuwabara, S. 1959 The forces experienced by randomly distributed parellel circular cylinders or spheres in a viscous flow at small reynolds numbers. *J. Phys. Soc. Jpn* **14**, 527–532.

Larson, R. G. 1999 *The Structure and Rheology of Complex Fluids*. Oxford University Press.

Lee, E., Chih, M. H. & Hsu, J. P. 2001 Conductivity of a concentrated spherical colloidal dispersion. *J. Phys. Chem.* B **105**, 747–753.

Levine, S. & Neale, G. H. 1974 Prediction of electrokinetic phenomena within multiparticle systems. Part 1. Electrophoresis and electroosmosis. *J. Colloid Interface Sc.* **47**, 520–529.

Levine, S., Neale, G. & Epstein, N. 1976 Prediction of electrokinetic phenomena within multiparticle systems. *J. Colloid Interface Sci.* **57**, 424–437.

Lin, H., Storey, B. D., Oddy, M. H., Chen, C. H. & Santiago, J. G. 2004 Instability of electrokinetic microchannel flows with conductivity gradients. *Phys. Fluids* **16**, 1922–1935.

Lyklema, J. 2005 *Fundamentals of Interface and Colloid Science*. Elsevier Academic Press.

Mangelsdorf, C. S. & White, L. R. 1990 Effects of stern-layer conductance on electrokinetic transport-properties of colloidal particles. *J. Chem. Soc., Faraday Trans.* **86**, 2859–2870.

Maxwell, J. C. 1873 *Electricity and Magnetism.* Oxford University. Press.

McKenzie, D. R., McPhedran, R. C. & Derrick, G. H. 1978 Conductivity of lattices of spheres. Part 2. Body-centered and face-centered cubic lattices. *Proc. R. Soc. Lond.* A **362**, 211–232.

Melcher, J. R. & Taylor, G. I. 1969 Electrohydrodynamics: a review of the role of interfacial shear stress. *Ann. Rev. Fluid Mech.* **1**, 111–146.

Mooney, M. 1951 The viscosity of a concentrated suspension of spherical particles. *J. Colloid Sci.* **6**, 162.

Navaneetham, G. 2007 *Electrokinetic Instabilities in Non-Dilute Colloidal Suspensions.* Arizona State University.

Obrien, R. W. 1981 The electrical-conductivity of a dilute suspension of charged-particles. *J. Colloid Interface Sci.* **81**, 234–248.

Obrien, R. W. 1983 The solution of the electrokinetic equations for colloidal particles with thin double-layers. *J. Colloid Interface Sci.* **92**, 204–216.

Obrien, R. W. & White, L. R. 1978 Electrophoretic mobility of a spherical colloidal particle. *J. Chem. Soc. Faraday Trans.* **74**, 1607–1626.

Oddy, M. H. & Santiago, J. G. 2005 Multiple-species model for electrokinetic instability. *Phys. Fluids* **17**, 064108-1 to 064108-17.

Oddy, M. H., Santiago, J. G. & Mikkelsen, J. C. 2001 Electrokinetic instability micromixing. *Analyt. Chem.* **73**, 5822–5832.

Ohshima, H. 1999 Electrical conductivity of a concentrated suspension of spherical colloidal particles. *J. Colloid Interface Sci.* **212**, 443–448.

Ohshima, H. 2000 Electrical conductivity of a concentrated suspension of soft particles. *J. Colloid Interface Sci.* **229**, 307–309.

Ohshima, H., Healy, T. W. & White, L. R. 1983 Approximate analytic expressions for the electrophoretic mobility of spherical colloidal particles and the conductivity of their dilute suspensions. *J. Chem. Soc., Faraday Trans.* **79**, 1613–1628.

O'Konski, C. T. 1960 Electric properties of macromolecules. Part 5 Theory of ionic polarizations in polyelectrolytes. **64**, 605–619.

Overbeek, J. T. 1950 Quantitative interpretation of the electrophonetic velocity of colloids. *Advan. Colloid Sci.* **3**, 97.

Ozen, O., Aubry, N., Papageorgiou, D. T. & Petropoulos, P. G. 2006 Electrohydrodynamic linear stability of two immiscible fluids in channel flow. *Electrochim. Acta* **51**, 5316–5323.

Perez, A. T. & Lemaire, E. 2004 Measuring the electrophoretic mobility of concentrated suspensions in nonaqueous media. *J. Colloid Interface Sci.* **279**, 259–265.

Posner, J. D. & Santiago, J. G. 2006 Convective instability of electrokinetic flows in a cross-shaped microchannel. *J. Fluid Mech.* **555**, 1–42.

Preisler, J. & Yeung, E. S. 1996 Characterization of nonbonded poly(ethylene oxide) coating for capillary electrophoresis via continuous monitoring of electroosmotic flow. *Analyt. Chem.* **68**, 2885–2889.

Probstein, R. F. 1994 *Physicochemical Hydrodynamics: An Introduction.* John Wiley.

Rosen, L. A. & Saville, D. A. 1991 Dielectric-spectroscopy of colloidal dispersions: Comparisons between experiment and theory. *Langmuir* **7**, 36–42.

Russel, W. B., Saville, D. A. & Schowalter, W. R. 1989 *Colloidal Dispersions.* Cambridge University Press.

Saffman, P. G. & Taylor, G. 1958 The penetration of a fluid into a porous medium or hele-shaw cell containing a more viscous liquid. *Proc. R. Soc. Lond.* A **245**, 312–&.

Sangani, A. S. & Acrivos, A. 1983 The effective conductivity of a periodic array of spheres. *Proc. R. Soc. Lond.* A **386**, 263–275.

Saville, D. A. 1979 Electrical-conductivity of suspensions of charged-particles in ionic-solutions. *J. Colloid Interface Sci.* **71**, 477–490.

Saville, D. A. 1997 Electrohydrodynamics: the Taylor–Melcher leaky dielectric model. *Ann. Rev. Fluid Mech.* **29**, 27–64.

Sigurdson, M., Wang, D. & Meinhart, C. D. 2005 Electrothermal stirring for heterogeneous immunoassays. *Lab Chip* **5**, 1366–1373.

Simha, R. 1940 The influence of brownian movement on the viscosity of solutions. *J. Phys. Chem.* **44**, 25.

Smoluchowski, M. 1918 Versuch einer mathematischen theorie der koagulationskinetik koiloider lösungen. *Z. Phys. Chem.* **92**, 129.

Stone, H. A. & Kim, S. 2001 Microfluidics: basic issues, applications, and challenges. *Aiche J.* **47**, 1250–1254.

Storey, B. D., Tilley, B. S., Lin, H. & Santiago, J. G. 2005 Electrokinetic instabilities in thin microchannels. *Phys. Fluids* **17**, 018103-1 to 018103-4.

Stratton, J. A. 1941 *Electromagnetic Theory*. McGraw-Hill.

Tirado, M. C., Arroyo, F. J., Delgado, A. V. & Grosse, C. 2000 Measurement of the low-frequency dielectric properties of colloidal suspensions: comparison between different methods. *J. Colloid Interface Sci.* **227**, 141–146.

Trau, M., Sankaran. S., Saville. D. A. & I. A., A. (1995). Electric field induced pattern formations in colloidal dispersions. *Nature* **374**, 437–439.

Trau, M., Saville, D. A. & Aksay, I. A. 1996 Field-induced layering of colloidal crystals. *Science* **272**, 706–709.

Vand, V. 1948 Viscosity of solutions and suspensions. Part 2. *J. Phys. Chem.* **52**, 277.

Voegtli, L. P. & Zukoski, C. F. 1991 Adsorption of ionic species to the surface of polystyrene latexes. *J. Colloid Interface Sci.* **141**, 92–108.

Watillon, A. & Stone-Masui, J. 1972 Surface conductance in dispersions of spherical particles – study of monodisperse polystyrene latices. *J. Electroanalyt. Chem.* **37**, 143–160.

Wereley, S. T., Meinhart, C. D., Santiago, J. G. & Adrian, R. J. 1998 Velocimetry for mems applications. In *Proc. ASME/DSC (Micro-Fluidics Symposium)*, Anaheim, CA, USA.

Whitesides, G. M. & Grzybowski, B. 2002 Self-assembly at all scales. *Science* **295**, 2418–2421.

Wiersema, P. H., Loeb, A. L. & Overbeek, J. T. 1966 Calculation of electrophoretic mobility of a spherical colloid particle. *J Colloid Interface Sci.* **22**, 78-&.

Zukoski, C. F. & Saville, D. A. 1985 An experimental test of electrokinetic theory using measurements of electrophoretic mobility and electrical-conductivity. *J Colloid Interface Sci.* **107**, 322–333.

Zukoski, C. F. & Saville, D. A. 1986 The interpretation of electrokinetic measurements using a dynamic-model of the stern layer. Part 1. The dynamic-model. *J. Colloid Interface Sci.* **114**, 32–44.

Zukoski, C. F. & Saville, D. A. 1987 Electrokinetic properties of particles in concentrated suspensions. *J. Colloid Interface Sci.* **115**, 422–436.

Zukoski, C. F. & Saville, D. A. 1989 Electrokinetic properties of particles in concentrated suspensions–heterogeneous systems. *J. Colloid Interface Sci.* **132**, 220–229.